Inorganic Chemistry

ARTICLE

pubs.acs.org/IC

DFT Calculations for Intermediate and Active States of the Diiron Center with a Tryptophan or Tyrosine Radical in *Escherichia coli* Ribonucleotide Reductase

Wen-Ge Han and Louis Noodleman*

Department of Molecular Biology, TPC15, The Scripps Research Institute, 10550 North Torrey Pines Road, La Jolla, California 92037, United States

Supporting Information

ABSTRACT: Class Ia ribonucleotide reductase subunit R2 contains a diiron active site. In this paper, active-site models for the intermediate X-Trp48$^{\bullet+}$ and X-Tyr122$^{\bullet}$, the active Fe(III)Fe(III)-Tyr122$^{\bullet}$, and the met Fe(III)Fe(III) states of *Escherichia coli* R2 are studied, using broken-symmetry density functional theory incorporated with the conductor-like screening solvation model. Different structural isomers and different protonation states have been explored. Calculated geometric, energetic, Mössbauer, hyperfine, and redox properties are compared with available experimental data. Feasible detailed structures of these intermediate and active states are proposed. Asp84 and Trp48 are most likely the main contributing residues to the result that the transient Fe(IV)Fe(IV) state is not observed in wild-type class Ia *E. coli* R2. Asp84 is proposed to serve as a proton-transfer conduit between the diiron cluster and Tyr122 in both the tyrosine radical activation pathway and the first steps of the catalytic proton-coupled electron-transfer pathway. Proton-coupled and simple redox potential calculations show that the kinetic control of proton transfer to Tyr122$^{\bullet}$ plays a critical role in preventing reduction from the active Fe(III)Fe(III)-Tyr122$^{\bullet}$ state to the met state, which is potentially the reason why Tyr122$^{\bullet}$ in the active state can be stable over a very long period.

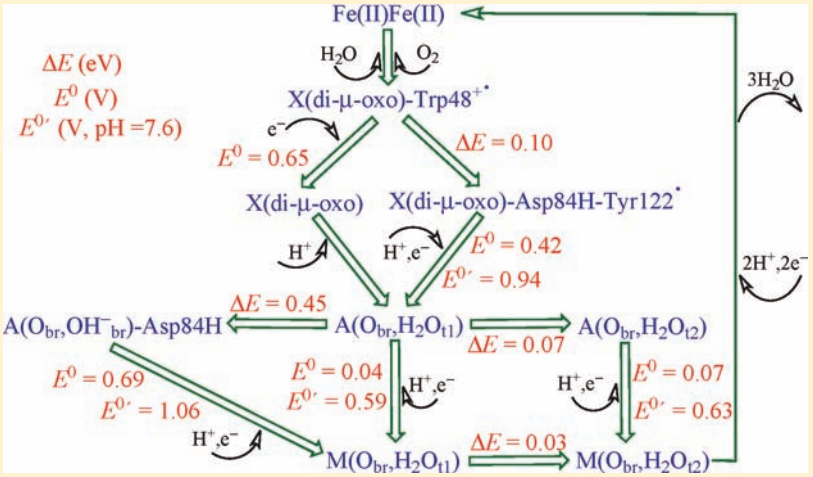

1. INTRODUCTION

Ribonucleotide reductases (RNRs) catalyze the reduction of ribonucleotides to deoxyribonucleotides, providing the required building blocks for DNA replication and repair.[1,2] Class Ia RNRs consist of two dissimilar protein subunits, R1 and R2, each a homodimer in an overall $\alpha_2\beta_2$ architecture. The ribonucleotide-to-deoxyribonucleotide reactions occur by a long-range radical (or a proton-coupled electron-transfer) propagation mechanism initiated by a fairly stable tyrosine radical (Tyr122 in *Escherichia coli*) in subunit R2, where a dinuclear iron cluster initially generates and stabilizes this tyrosine radical. The subunit R1 contains the substrate binding site and catalyzes dehydroxylation of the 2′-hydroxyl group of the ribose ring. The tyrosine radical in R2 has been identified in the neutral deprotonated form with the oxidized Fe(III)Fe(III) active site and is stable for days at room temperature.[1] Once this tyrosine radical is lost, the enzyme becomes inactive. The active form can be regenerated by a complicated sequence of steps involving changes in the oxidation state and structural rearrangement with coupled electron and proton transfers (see Figure 1). First, the resting oxidized diferric met form of R2 ($R2_{ox(met)}$)[3] is reduced by two electrons from a reductase protein to the diferrous form, $R2_{red}$.[4] Next, molecular oxygen (O_2) binds to the diiron center of $R2_{red}$ and the O−O bond breaks. Then, a high-oxidation intermediate state of RNR-R2, called X, is kinetically and spectroscopically observed.[5−10] A combination of Q-band electron−nuclear double resonance (ENDOR) and Mössbauer data on a Y122F-R2 mutant indicates that the iron centers of X are high-spin Fe(III) ($S = {}^5/_2$) and high-spin Fe(IV) ($S = 2$) sites that antiferromagnetically (AF) couple to give an $S_{total} = {}^1/_2$ ground state.[10] The formation of X requires an extra electron, evidently coming from a tryptophan residue because a transient, broad absorption band centered near 560 nm develops upon the reaction of O_2 with the Fe(II)Fe(II) cluster and is ascribed to a tryptophan cation radical.[11,12] Such a transient 560 nm absorption is not observed in the reaction of

Received: October 1, 2010
Published: February 15, 2011

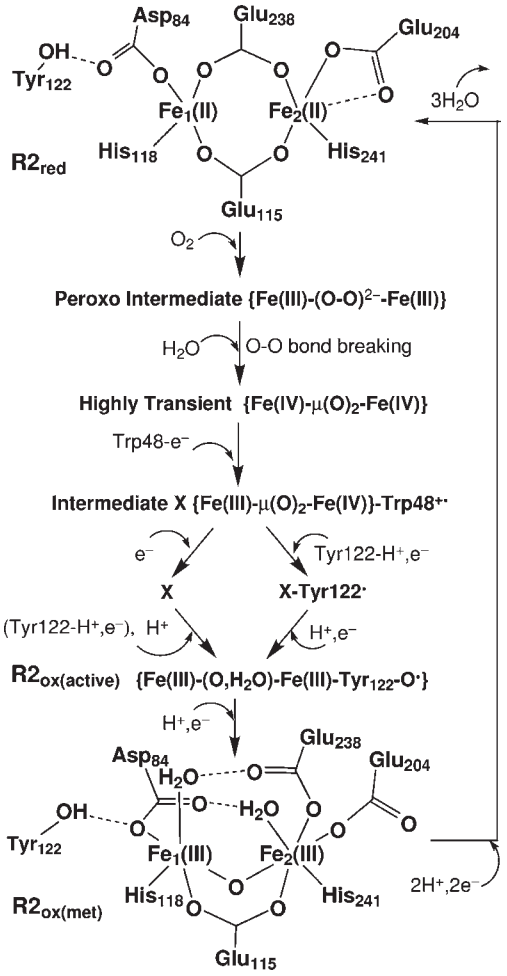

Figure 1. Schematic drawing of the processing cycle of reproducing Tyr122• from the met diferric state of *E. coli* R2.

E. coli W48F mutant R2, which provides strong evidence that Trp48 in *E. coli* is the donor of the extra electron.[12] Further evidence for the assignment of Trp48•+ is the acceleration of decay of the 560-nm-absorbing species by ascorbate, free Fe(II), and 2-mercaptoethanol[11] because Trp48 is near the surface of the protein and is in the hydrogen-bonding network of Tyr122···Asp84···Fe1···His118···Asp237···Trp48, where Fe1 is the iron site closer to Tyr122.

If Trp48•+ is reduced by a nearby reductant, the intermediate X-Fe(III)Fe(IV) is the species that oxidizes Tyr122 to Tyr122•. RNR-X has captured the attention of many researchers over the past decade to elucidate its chemical and structural nature.[5−35]

In the absence of a reductant near Trp48•+, Tyr122• can be produced by an electron-transfer reaction to Trp48•+, and this Tyr122• forms faster than that produced by X alone.[11] The generation of Tyr122• by Trp48•+ of the X-Trp48•+ species then produces an intermediate containing both X and Tyr122•. A related species accumulates in the electron-deficient W48F-R2 reaction, enough to allow its spectroscopic characteristics to be determined.[12]

Presently, the detailed structures for the intermediates X-Trp48•+ and X-Tyr122• and the active diferric form of R2, which contains the tyrosine radical, are not known. However, the reduced diferrous[4] and met oxidized diferric[3] (without Tyr122•) states of *E. coli* R2 have been crystallized, and their X-ray

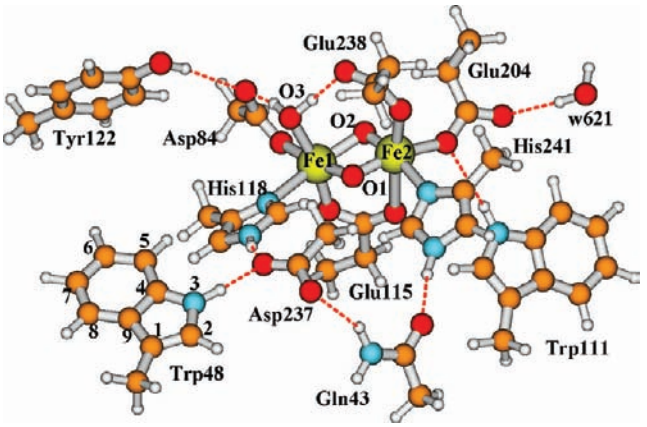

Figure 2. Our previously proposed *E. coli* RNR-X active-site structure with a di-μ-oxo bridge.[27] This is also our currently proposed structure for the X-Trp48•+ state and for the possible Fe1(IV)Fe2(IV) state.

structures were determined at 1.7 and 2.2 Å resolution, respectively. In this paper, on the basis of the active-site crystal structures of the Fe(II)Fe(II) and Fe(III)Fe(III) clusters and earlier proposed RNR-X active-site models,[27,30] we will study feasible active-site structures of the X-Trp48•+, X-Tyr122•, and active Fe(III)Fe(III)-Tyr122• states using broken-symmetry (BS)[36−38] density functional theory (DFT) calculations.

2. ACTIVE-SITE MODELS

The diiron centers of the reduced and oxidized (met) *E. coli* R2 X-ray crystal structures are schematically shown in Figure 1. In both states, the −OH group of Tyr122 hydrogen bonds with the Asp84 side chain. Fe1 (which is closer to Tyr122) is ligated to the side chains of Asp84 and His118, and the other iron (Fe2) is ligated to Glu204 and His241. In the reduced diferrous cluster, both carboxylate groups from Glu238 and Glu115 exist in a bridging position between the two irons. In the diferric (met) center, the carboxylate of Glu238 changes from the bidentate position to monodentate binding with only Fe2, and each iron site has a terminally binding water molecule, which also hydrogen bonds with Glu238 and Asp84, respectively. In the outer ligand shells, the main hydrogen-bonding interactions between the residue side chains are (see Figure 2) as follows: Trp111···Glu204, His118···Asp237···Trp48, and Asp237···Gln43···His241. The Tyr122···Asp84−Fe1−His118···Asp237···Trp48 pathway is designed for the electron transfer and creation of the Trp48•+ and Tyr122• radicals.

Upon O_2 binding to the Fe(II)Fe(II) center, a diferric peroxo intermediate state (P) was observed in the D84E mutant[39] and W48F/D84E double mutant R2.[40] Very recently, Jensen et al. performed a series of DFT calculations and proposed that O_2 binds to the diferrous center in a cis-μ-1,2 mode,[41] which is consistent with our previous calculations for the peroxo intermediate P of methane monooxygenase (MMO).[42] Structural changes along with electron/proton transfers should occur after O_2 binding with Fe(II)Fe(II). A water molecule is proposed to enter along with O_2 and binds to the Fe1 site, which causes the opening of the bridging carboxylate of Glu238 to a monodentate binding position with Fe2 and hydrogen bonding with this H_2O.[41] Meanwhile, the Asp84 side chain rotates, so that one of its oxygen atoms hydrogen bonds to both Tyr122 and the terminal water on Fe1. This process possibly generates another

dx.doi.org/10.1021/ic1020127 |*Inorg. Chem.* 2011, 50, 2302–2320

peroxo-type intermediate state P′ proposed by Jensen et al.,[41] which falls between intermediate P and X and has been observed in the RNR W48A/Y122F double mutant.[43] Next, the O−O bond breaks, an electron transfers from Trp48 to one of the iron sites, and X{Fe(III)Fe(IV)}-Trp48$^{\bullet+}$ is formed.

In recent years, our group has been studying the properties of a set of active-site model clusters for RNR-X using BS DFT methods[25−31] and have compared them with the available experimental data, including Mössbauer,[10] ^{57}Fe, ^{1}H, $^{17}O_2$, and $H_2{}^{17}O$ ENDOR,[17,19,20] extended X-ray absorption fine structure (EXAFS),[18] and magnetic circular dichroism (MCD).[21] We have performed these calculations on a wide variety of RNR-X model systems [many with both Fe1(III)Fe2(IV) and Fe1(IV)Fe2(III) comparisons] including "open" systems with a single μ-oxo bridge or a μ-oxo and μ-1,1 carboxylate bridge (in addition to the μ-1,3 carboxylate bridge from Glu115 usually present) and on more "closed" complexes with either a $(\mu\text{-oxo})_2$ or a (μ-oxo)(μ-hydroxo) bridge. The open systems display a very long Fe−Fe bond length, >2.9 Å (much longer than that from EXAFS analysis), poor ^{57}Fe Mössbauer properties, and poor ^{17}O and ^{1}H parameters compared to those observed for ENDOR spectra.[19] Based on the detailed analysis and comparisons, the model we studied that can best reproduce most of the experimentally observed properties, in particular the ENDOR experiments,[19,20] contains (Figure 2) two μ-oxo bridges (O1 and O2), plus one terminal water (O3) that binds to Fe1(III) and also hydrogen bonds to both side chains of Asp84 and Glu238, and one bidentate carboxylate group from the side chain of Glu115.[27,29]

On the other hand, Mitić et al. performed Fe(IV) d−d transition calculations using time-dependent DFT (TD-DFT) on their RNR-X models and compared them with their MCD experiments.[35] They found that the assignment of the Fe(IV) d−d transitions in wild-type RNR-X best correlates with the Fe(III)(μ-O)(μ-OH)Fe(IV) structure, which differs from the di-μ-oxo model only by having a proton on the bridging oxygen-labeled O2. However, the newly performed ENDOR experiments by Shanmugam et al.[20] ruled out the μ-hydroxo bridge in X. The authors have proposed that X contains a μ-oxo bridge and a terminal hydroxo bound to Fe(III).[20] A model of this type in our previous calculations[27] shows poor ^{57}Fe Mössbauer parameters and also poor ^{1}H hyperfine parameters compared to ^{1}H ENDOR.[19] In the current paper, we therefore started from our previously calculated X(di-μ-oxo) model (Figure 2) to establish the current X-Trp48$^{\bullet+}$ and X-Tyr122$^{\bullet}$ models. Also, in our proposed reaction pathway, the external proton enters the active site after X (Figure 1, left-hand side).

Because the X-Trp48$^{\bullet+}$ state is 1+ more positive than the net charge of X, if the active site of X contains as alternative states di-μ-oxo (Figure 2) or (μ-oxo, μ-hydroxo), the center of X-Trp48$^{\bullet+}$ is likely to have the di-μ-oxo structure. We note that the total cluster charge, including only the first-shell ligands, is 1− for the di-μ-oxo structure and 0 for the (μ-oxo, μ-hydroxo) structure. To test this idea, we will first calculate the energetics of the X{Fe(III)(di-μ-oxo)Fe(IV)}-Trp48$^{\bullet+}$ and X{Fe(III)(μ-oxo, μ-hydroxo)Fe(IV)}-Trp48$^{\bullet+}$ structures. The initial geometries are taken from our previously optimized X model calculations,[31] which were originally constructed from chain A of the oxidized *E. coli* R2 (met) diferric [Fe(III)Fe(III)] X-ray crystal structure (PDB code: 1RIB),[3] by breaking the $C_\beta-C_\alpha$, $C_\gamma-C_\beta$, or $C_\delta-C_\gamma$ bonds and adding a linking hydrogen atom along the C−C direction to fill the open valence of the terminal carbon atom.[44] The reason for starting from the diferric X-ray crystal structure is that the overall protein structure and orientations of most of the carboxylate ligands of X should be closer to the diferric state than the diferrous state. The sizes of the active-site models in the current study are as shown in Figure 2, which is also the structure of the current X{Fe(III)(di-μ-oxo)Fe(IV)}-Trp48$^{\bullet+}$ model. Note that the X-Trp48$^{\bullet+}$ model studied by Siegbahn is the same as our X{Fe(III)(di-μ-oxo)Fe(IV)}-Trp48$^{\bullet+}$ model, but Siegbahn's model has a smaller size and an Fe1(IV)Fe2(III) assignment,[23,24] reversed from ours, Fe1(III)Fe2(IV), with the latter based on Bollinger's Mössbauer and kinetic experiments.[45] The X{Fe(III)(μ-oxo, μ-hydroxo)Fe(IV)}-Trp48$^{\bullet+}$ model is then constructed by adding a proton to the bridging oxygen O2.

The models of the X-Tyr122$^{\bullet}$ and active Fe(III)Fe(III)-Tyr122$^{\bullet}$ states from our current calculations are given in the Results and Discussion section.

3. COMPUTATIONAL METHODOLOGY

All DFT spin-unrestricted calculations have been performed using the Amsterdam Density Functional (ADF) package.[46−48] The parametrization of Vosko, Wilk, and Nusair (VWN)[49] is used for the local density approximation term, and the OPBE[50−52] functional is used for the nonlocal exchange and correlation terms. OPBE is a combination of Handy's optimized exchange (OPTX)[52] and PBE correlation (PBEc) functionals.[50,51]

In previous work,[25−29] we used the PW91 exchange-correlation potential[53] and established that, by comparison with experimental ^{57}Fe Mössbauer (isomer-shift and quadrupole-splitting parameters) and also ^{57}Fe ENDOR hyperfine parameters, the PW91 potential displays the experimentally correct high-spin Fe(III) and Fe(IV) sites in RNR-X. This correct spin-state character is also found in lower oxidation states for RNR, MMO, and related synthetic complexes. However, for the Fe(IV)Fe(IV) oxidation state of MMO (intermediate state Q), some structural models show incorrect spin-crossover behavior.[54] We addressed this problem by using OPBE for high-oxidation-state problems involving RNR and MMO. OPBE shows a considerably improved spin-state crossover energy balance for this class of systems.[30,54]

Swart et al. have reported a systematic study on the performance of several exchange-correlation functionals for seven different iron complexes that are experimentally found to have either a low-, intermediate-, or high-spin ground state.[55] They found that the OPTX functional performs well and the OPBE functional performs the best among general gradient approximation (GGA)-type potentials. These authors have also tested different functionals in calculating the atomization energies for the G2 set of up to 148 molecules, six reaction barriers of S_N2 reactions, geometry optimizations of 19 small molecules and 4 metallocenes, and zero-point vibrational energies for 13 small molecules.[56] Their examination shows that the OPTX functionals perform better than the regular GGAs like PBE,[50,51] BLYP,[57,58] and BP,[57,59,60] and OPBE performs exceptionally well in all cases. Recently, new functionals like the double-hybrid B2PLYP[61] and hybrid meta-GGA functional TPSSh[62] have been demonstrated to outperform the hybrid B3LYP[58,63,64] and nonhybrid functionals for predicting certain properties for test sets of transition-metal systems.[65−68] However, Mössbauer isomer shift parameters for the latter potentials have not yet been fitted for the Fe-oxo complexes. The extensive family of geometry optimizations within the dielectric continuum solvation model in the current study is also difficult with hybrid functionals because our models are large (over 140 atoms), and hybrid or meta-hybrid methods require about 3 times the computer time of regular GGA methods. We therefore continue to use the OPBE potential in the current study for both geometry optimization and Mössbauer property calculations.

Bollinger et al. proposed that site Fe1, which is closer to Tyr122, is the ferric site in RNR-X based on their two-iron-isotope reactions and

Table 1. Calculated Fe−Fe and Fe−Ligand Distances (Å), the Net Spin Populations (NSPs) of Fe1(III), Fe2(IV), and Trp48$^{\bullet+}$, the BS State Energies E (eV), and the pK_a Value of the Bridging O2 Site for Models X(di-μ-oxo)-Trp48$^{\bullet+}$ and X(μ-oxo)(μ-hydroxo)-Trp48$^{\bullet+}$ and Similar Calculated Properties for Fe1(IV)(di-μ-oxo)Fe2(IV)[a]

	X(di-μ-oxo)-Trp48$^{\bullet+}$		X(μ-oxo)(μ-hydroxo)-Trp48$^{\bullet+}$	Fe1(IV)(di-μ-oxo)Fe2(IV)
	S_{total} = 0	S_{total} = 1	S_{total} = 0	S_{total} = 0
Fe1−Fe2	2.792	2.794	2.959	2.731 (2.744) [b]
Fe1−O1	1.886	1.926	1.934	1.765 (1.772)
Fe2−O1	1.748	1.732	1.708	1.815 (1.808)
Fe1−O2	1.937	1.968	2.153	1.832 (1.809)
Fe2−O2	1.758	1.753	1.960	1.769 (1.786)
Fe1−O3	2.119	2.130	2.092	2.125 (2.095)
Fe1−N−His118	2.345	2.368	2.196	2.180 (2.212)
Fe2−N−His241	2.180	2.192	2.154	2.102 (2.155)
Fe1−O−Asp84	2.081	2.117	2.019	1.958 (2.001)
Fe1−O−Glu115	1.985	1.995	1.980	2.020 (2.012)
Fe2−O−Glu115	2.592	2.598	2.350	2.349 (2.344)
Fe2−O−Glu204	1.964	1.986	1.922	1.923 (1.910)
Fe2−O−Glu238	2.065	2.075	2.013	2.049 (2.037)
NSP(Fe1)	3.83	4.04	4.09	3.15 (3.14)
NSP(Fe2)	−3.24	−3.23	−3.28	−3.17 (−3.16)
NSP(C1-Trp48$^{\bullet+}$)	−0.24	0.24	−0.43	0.00
NSP(C2-Trp48$^{\bullet+}$)	−0.07	0.07	−0.14	0.00
NSP(N3-Trp48$^{\bullet+}$)	−0.09	0.09	−0.14	0.00
NSP(C4-Trp48$^{\bullet+}$)	−0.01	0.01	−0.03	0.00
NSP(C5-Trp48$^{\bullet+}$)	−0.04	0.04	−0.05	0.00
NSP(C6-Trp48$^{\bullet+}$)	−0.08	0.09	−0.16	0.00
NSP(C7-Trp48$^{\bullet+}$)	0.03	−0.03	0.06	0.00
NSP(C8-Trp48$^{\bullet+}$)	−0.12	0.13	−0.22	0.00
NSP(C9-Trp48$^{\bullet+}$)	0.05	−0.05	0.10	0.00
E	−880.6840	−880.5995	−880.4384	−880.9702 (−880.8538)
pK_a [c]			6.06	

[a] The models of X(di-μ-oxo)-Trp48$^{\bullet+}$ and Fe1(IV)(di-μ-oxo)Fe2(IV) are shown in Figure 2. The difference between X(di-μ-oxo)-Trp48$^{\bullet+}$ and X(μ-oxo)(μ-hydroxo)-Trp48$^{\bullet+}$ is that the bridging site O2 is protonated in X(μ-oxo)(μ-hydroxo)-Trp48$^{\bullet+}$. [b] Data in parentheses are for the geometry that was optimized starting from the S_{total} = 0 state X(di-μ-oxo)-Trp48$^{\bullet+}$ optimized geometry, and all of the hydrogen-linking atoms were fixed according to the initial geometry during the optimization process. [c] For the process given in eq 4 and calculated according to eq 5 using S_{total} = 0 state (BS M_s = 0) energies.

Mössbauer spectroscopy experiments.[45] This conclusion is supported by our previous ^{1}H and ^{17}O hyperfine **A**-tensor calculations for the water ligand (bound to Fe1) in X active-site models[27,29] and is consistent with the internal electron transfer from Trp48 along the Trp48···Asp237···His118···Fe1 hydrogen-bonding pathway. In the current study, we will only perform calculations on the Fe1(III)Fe2(IV) high-spin AF-coupled (S_1 = $^5/_2$, S_2 = 2, and S_X = $^1/_2$) state for the X center. X-Trp48$^{\bullet+}$ and X-Tyr122$^{\bullet}$ are diradicals. The total spin of these diradicals can be either 0 or 1. As in previous work, we will perform BS[36−38] calculations to represent these spin states. First, we construct a ferromagnetically (F) spin-coupled (S_{total} = $^{10}/_2$ for X-Trp48$^{\bullet+}$ or X-Tyr122$^{\bullet}$) determinant, where the spins on both irons and on Trp48$^{\bullet+}$ or Tyr122$^{\bullet}$ are aligned in a parallel fashion. Then, we rotate the spin vector located on atom Fe1(III) or atom Fe2(IV) by interchanging the α and β fit density blocks on site Fe1 or Fe2 from the output file TAPE21 created by this F-coupled calculation in ADF to get the starting spin density for the S_{total} = 0 [flip Fe1(III)] or S_{total} = 1 [flip Fe2(IV)] diradical state. These BS states are not pure S_{total} = 0 or S_{total} = 1 states. Instead, these BS states (and their energies) are weighted averages of the pure spin states, strongly weighted toward the lower S_{total} states based on the spin-coupling algebra.[36−38] We have not included spin-projection corrections in the current work because we have estimated that these will make only very small differences in the DFT-calculated relative energies of different states. The properties of BS states can be directly connected to the hyperfine properties of corresponding pure spin states using the Wigner−Eckart theorem.[36−38,67]

3.1. Geometry Optimization. All models are optimized within the conductor-like screening (COSMO)[69−72] solvation model with dielectric constant ε = 20. In COSMO, the quantum cluster is embedded in a molecular-shaped cavity surrounded by a continuum dielectric medium. There is no universal dielectric constant for COSMO-like solvation calculations. Although the dielectric value ε = 4 is commonly used for the protein interior, because this is the value of the dielectric constants of crystalline and polymeric amides[73] and dry protein and peptide powders,[74−77] many studies show that higher effective dielectric constant values (4−30) for protein interiors are needed to reproduce the pK_a values of certain internal ionizable groups.[77−84] Very recently,[31] we have studied the quantum cluster size and solvent polarity effects on the geometries and Mössbauer properties of RNR-X(di-μ-oxo) models. Our calculations show that certain Fe−ligand distances [especially Fe1−N(His118) in X], Mössbauer quadruple splittings, and Heisenberg J coupling constants are sensitive to both the quantum cluster size and polarity of the environment, while the calculated Mössbauer isomer shift and various hyperfine **A**-tensor properties change very little with the

dx.doi.org/10.1021/ic1020127 |Inorg. Chem. 2011, 50, 2302–2320

model size and ε.[31] $\varepsilon = 4$ appears to be too small when for the study of the diiron active-site geometry with only the first-shell ligands, as seen by comparison with larger models. In the current study, the diradical state can be difficult to obtain, and geometry optimizations are time-consuming. We therefore choose a medium model size for the quantum cluster (Figure 2), which contains up to the second-shell residue side chains (and including also Trp48 and Gln43, third-shell residue side chains) around the diiron center. Accordingly, we choose a larger dielectric constant ($\varepsilon = 20$) for the current calculations in COSMO. The van der Waals radii for iron, carbon, oxygen, nitrogen, and hydrogen atoms are taken as 1.5, 1.7, 1.4, 1.55, and 1.2 Å, respectively. The probe radius for the contact surface between the cluster and solvent is set to 2.0 Å. The triple-ζ polarization (TZP) Slater-type basis sets with frozen cores [C(1s), N(1s), O(1s), and Fe(1s,2s,2p) are frozen] are applied for geometry optimizations. The linking hydrogen atoms on Tyr122, Gln43, Trp48, and Trp111 are fixed during geometry optimizations. The BS state energies obtained after COSMO geometry optimizations are used to compare the relative energies and calculate the redox potentials and pK_a's in the current paper. We understand that, depending on the systems and the DFT functionals employed, the entropy terms may also be significant in determining the relative free energies and the spin state.[85−87] However, frequency calculations within the COSMO solvation model for our current active-site clusters are very demanding. Further, the vibrational entropy terms obtained from frequency calculations are not accurate because the positions of certain linking hydrogen atoms are fixed during geometry optimizations. Unlike zero-point energies (ZPE), vibrational entropies are most sensitive to low-frequency modes, which are more difficult to calculate accurately. The constraints applied for geometry optimizations would need to be released or somehow modeled. We therefore did not calculate the entropy terms in the current study.

3.2. Mössbauer Isomer-Shift and Quadrupole-Splitting Calculations. For certain models and states, we have applied single-point Mössbauer isomer-shift and quadruple-splitting calculations at the optimized geometries using all-electron (i.e., without frozen-core approximation) TZP Slater-type basis sets. First, a high-spin F-coupled single-point energy calculation (in COSMO) is performed at the BS optimized geometry. Its TAPE21 file is then modified accordingly by interchanging the α and β fit density blocks on site Fe1 or Fe2. Starting from the modified TAPE21, a BS state single-point energy calculation in COSMO again with all-electron TZP Slater-type basis sets is performed to obtain the electron density [$\rho(0)$] and the electric field gradient (EFG) at the Fe nucleus.

The Mössbauer isomer shifts δ are calculated based on $\rho(0)$:

$$\delta = \alpha[\rho(0) - A] + C \quad (1)$$

In our previous studies,[54,88] the parameters α and C have been fitted separately for the $Fe^{2+,2.5+}$ and $Fe^{2.5+,3+,3.5+,4+}$ complexes for PW91, OPBE, and OLYP, with all-electron TZP Slater-type basis sets. For the $Fe^{2.5+,3+,3.5+,4+}$ complexes, we have obtained $A = 11\,877.0$, $\alpha = -0.312$, and $C = 0.373$ mm s^{-1} for the OPBE potential.

For calculation of the Mössbauer quadrupole splittings (ΔE_Q), the EFG tensors V are diagonalized and the eigenvalues are reordered so that $|V_{zz}| \geq |V_{xx}| \geq |V_{yy}|$. The asymmetry parameter η is defined as

$$\eta = |(V_{xx} - V_{yy})V_{zz}| \quad (2)$$

Then ΔE_Q for ^{57}Fe of the nuclear excited state ($I = {}^3/_2$) can be calculated as

$$\Delta E_Q = \left(\frac{1}{2}\right) eQV_{zz}(1 + \eta^2/3)^{1/2} \quad (3)$$

where e is the electrical charge of a positive electron and Q is the nuclear quadrupole moment (0.15 barns) of iron.[89]

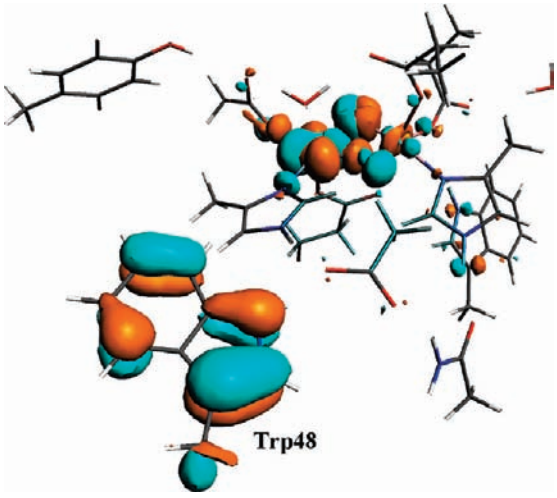

Figure 3. Molecular orbital plot for the virtual α-LUMO of the X(di-μ-oxo)-Trp48$^{\bullet+}$ model in the $S_{total} = 0$ state. A total of 50% of this orbital is located at Trp48.

3.3. pK_a Calculations. Several pK_a calculations are performed in the current paper. For example, to examine whether the (di-μ-oxo) or (μ-oxo)(μ-hydroxo) model for X-Trp48$^{\bullet+}$ is energetically more favored, we need to calculate the pK_a value for the bridging site O2. For the process

$$X(\mu\text{-oxo})(\mu\text{-hydroxo})\text{-Trp48}^{\bullet+} \rightarrow X(\text{di-}\mu\text{-oxo})\text{-Trp48}^{\bullet+} + H^+ \quad (4)$$

the pK_a value for the bridging OH^- group at site O2 is calculated by

$$\begin{aligned} 1.37\text{p}K_a &= E[X(\text{di-}\mu\text{-oxo})\text{-Trp48}^{\bullet+}] \\ &- E[X(\mu\text{-oxo})(\mu\text{-hydroxo})\text{-Trp48}^{\bullet+}] + E(H^+) \\ &+ \Delta G_{sol}(H^+, 1\text{ atm}) - T\Delta S_{gas}(H^+) + \Delta ZPE + \frac{5}{2}RT \end{aligned} \quad (5)$$

For the current study, the energies E[X(di-μ-oxo)-Trp48$^{\bullet+}$] and E[X(μ-oxo)(μ-hydroxo)-Trp48$^{\bullet+}$] are taken from the BS state energies after the COSMO geometry optimizations. $\Delta G_{sol}(H^+, 1\text{ atm})$ is the solvation free energy of a proton at 1 atm of pressure. We will use −263.98 kcal mol^{-1} [90−92] for this term because so far it is the best measured value (note that previously we used −262.11 kcal mol^{-1}, which was obtained from experimental and theoretical analysis[27]). $E(H^+) = 12.6416$ eV is the calculated energy of a proton (in the gas phase with the OPBE potential) with respect to a spin-restricted hydrogen atom. The translational entropy contribution to the gas-phase free energy of a proton is taken as $-T\Delta S_{gas}(H^+) = -7.76$ kcal mol^{-1} at 298 K and 1 atm of pressure.[93] $(5/2)RT$ includes the proton translational energy $(3/2)RT$ and $PV = RT$.[93] The zero-point-energy difference term ΔZPE is estimated as ΔZPE = −7.29 kcal mol^{-1} taken from previous frequency calculations for small X models.[30] Later, when we calculate the pK_a value for the Tyr122 side chain, ΔZPE is calculated separately and will be given in the text.

4. RESULTS AND DISCUSSION

4.1. Calculated Properties of Models X(di-μ-oxo)-Trp48$^{\bullet+}$ and X(μ-oxo)(μ-hydroxo)-Trp48$^{\bullet+}$ and the Possible Fe1-(IV)Fe2(IV) State. Table 1 shows the main calculated properties for the X(di-μ-oxo)-Trp48$^{\bullet+}$ and X(μ-oxo)(μ-hydroxo)-Trp48$^{\bullet+}$ models, including the Fe−Fe and main Fe−ligand distances (Å), the Mulliken net spin populations (NSPs) of Fe1(III), Fe2(IV), and Trp48$^{\bullet+}$, and the BS state energies E (eV) after COSMO optimizations.

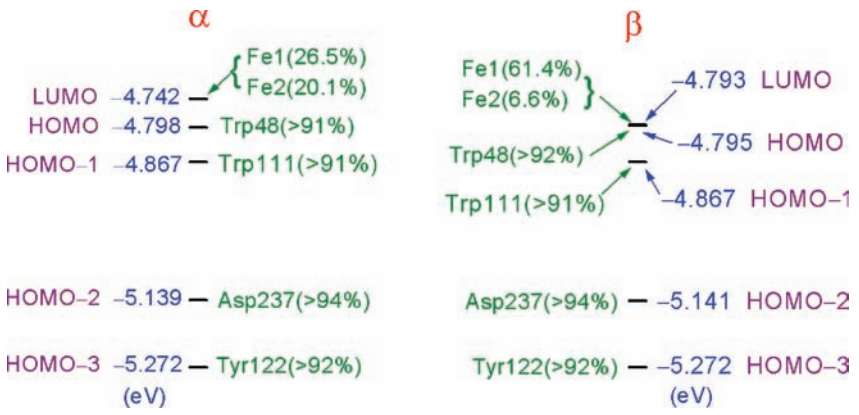

Figure 4. α and β molecular orbital energy (eV) levels around HOMO and LUMO for the Fe1(IV)(di-μ-oxo)Fe2(IV) model cluster. The atomic orbital contributions to the molecular orbital, which are larger than 1% and are located at the same residue side chain or at one of the iron sites, are added up to show the location of the molecular orbital. The majority spin is α on Fe1 and β on Fe2 (see Table 1).

The optimized geometries of X(di-μ-oxo)-Trp48$^{\bullet+}$ in the S_{total} = 0 and S_{total} = 1 states are very similar, except that the Fe1−O1 and Fe1−O2 distances in the S_{total} = 1 state are by 0.03−0.04 Å longer than the corresponding ones in the S_{total} = 0 state, resulting in a little larger NSP of Fe1 in the S_{total} = 1 state.

The NSPs are the main indications of the iron spin state and the free-radical location. In the ideal ionic limit, the net unpaired spin populations are 5 and 4 for the high-spin Fe1(III) (five d electrons) and Fe2(IV) (four d electrons) sites, respectively. The absolute calculated net spins in Table 1 are only smaller than the ionic limit by about one electron, indicating that the expected oxidation states of the iron sites with substantial Fe−ligand covalency are correctly predicted. The opposite signs for the spin densities of Fe1 and Fe2 confirm the AF coupling.

The calculated NSPs do show that the free radical is located at Trp48 for the X-Trp48$^{\bullet+}$ models. For model X(di-μ-oxo)-Trp48$^{\bullet+}$ in the S_{total} = 0 and S_{total} = 1 states, the total net spins on all of the carbon plus nitrogen atoms of the Trp48 ring is −0.57 (spin down) and 0.59 (spin up), respectively, clearly indicating that Trp48 is in the cation-radical state. Because the diiron center is far from Trp48 by ∼10 Å, the coupling between X and Trp48$^{\bullet+}$ is expected to be weak.[11] Our BS calculations do show the X(di-μ-oxo)-Trp48$^{\bullet+}$ models in the S_{total} = 0 and S_{total} = 1 states having similar energies, with the S_{total} = 0 state a little more stable than the S_{total} = 1 state by about 2 kcal mol^{-1}.

The atomic orbital contributions to the α-LUMO (lowest unoccupied molecular orbital) in the S_{total} = 0 state and the β-LUMO in the S_{total} = 1 state of the X(di-μ-oxo)-Trp48$^{\bullet+}$ model calculations also show that the electron hole mainly comes from Trp48 (see Figure 3).

We failed to converge the S_{total} = 1 state calculations for the X(μ-oxo)(μ-hydroxo)-Trp48$^{\bullet+}$ model. In Table 1, only the S_{total} = 0 state X(μ-oxo)(μ-hydroxo)-Trp48$^{\bullet+}$ calculated results were presented. It is reasonable to assume that its S_{total} = 0 state also has lower energy than (or very similar energy to) the S_{total} = 1 state. Compared with the X(di-μ-oxo)-Trp48$^{\bullet+}$ structures, the protonation of the bridging O2 site in X(μ-oxo)(μ-hydroxo)-Trp48$^{\bullet+}$ elongates the Fe−Fe distance, weakens the Fe1−O1 and Fe−O2 interactions, and strengthens all other Fe−ligand interactions. In the X(μ-oxo)(μ-hydroxo)-Trp48$^{\bullet+}$ model, the total NSP on the carbon and nitrogen atoms of the Trp48 ring is calculated to be −1.01 (spin down), indicating a very localized electron hole at Trp48.

According to eqs 4 and 5, we calculated the pK_a value for the bridging O2 site using the S_{total} = 0 BS state energies after the COSMO geometry optimizations. A pK_a value of 6.06 is obtained and is also given in Table 1. It is therefore the X(di-μ-oxo)-Trp48$^{\bullet+}$model in the S_{total} = 0 state that is more likely to represent the X-Trp48$^{\bullet+}$ active-site structure. This is also in agreement with analysis of the ^{2}H ENDOR measurements, indicating that X does not contain a μ-hydroxo bridge.[20]

Experimentally, it has been observed that the formation of X-Trp48$^{\bullet+}$ is kinetically first-order in both O_2 and the Fe(II)-R2 complex with a formation rate constant of ∼200 s^{-1}.[11] This implies that precursors to the X-Trp48$^{\bullet+}$ diradical species do not accumulate to greater than ∼10% of the initial Fe(II)-R2 reactant concentration.[11]

It is well-known that the hydroxylase component of MMO (MMOH) has a diiron active site similar to that of RNR-R2.[94] However, in MMOH, a glutamic acid residue, rather than aspartic acid (Asp84), binds to Fe1 (see Figure 2). Upon reaction with O_2, the O−O bond cleavage rate is only about 1 s^{-1},[95] and an intermediate state Q in MMOH has been kinetically and spectroscopically observed.[96−99] Q is proposed to be in the AF-coupled high-spin Fe1(IV)Fe2(IV) state with two di-μ-oxo bridges and one terminal water ligand, just as in the diiron center shown in Figure 2.[42,54,100,101] In MMOH, an arginine residue is in the place of Trp48 in *E. coli* R2.[94] Siegbahn performed the O−O bond cleavage calculations for the active sites of RNR-R2 and MMOH and concluded that electron transfer from Trp48 to the diiron center decreases the O−O cleavage barrier by approximately 3 kcal mol^{-1} for RNR compared to MMOH.[23,24] This electron transfer therefore possibly occurs sometime during the O−O bond cleavage, which explains the faster O−O cleavage rate in wild-type R2 than in MMOH. However, although with a slower rate, the O−O bond still can be cleaved in the W48F mutant R2.[12] It has been observed that, after O−O cleavage, a species that was proposed as the Fe(IV)O_2Fe(IV) state[12] is accumulated at the 80 s^{-1} rate.[12] Therefore, there is still some probability that the Fe(IV)Fe(IV) state, like intermediate Q in MMOH, is formed before the electron is transferred from Trp48 to the diiron center in wild-type R2. We present results on the structural, electronic, and energetic properties of the Fe(IV)Fe(IV) state and discuss why it is not observed in wild-type R2.

The Fe1(IV)Fe2(IV) state possibly has a structure similar to those of MMOH-Q[42,54] and X-Trp48$^{\bullet+}$, as shown in Figure 2.

dx.doi.org/10.1021/ic1020127 |*Inorg. Chem.* 2011, 50, 2302–2320

We therefore also optimized the geometry of the BS ($S_{total} = 0$) state of Fe1(IV)(di-μ-oxo)Fe2(IV), starting from the $S_{total} = 0$ X(di-μ-oxo)-Trp48$^{\bullet+}$ structure. The geometric and energetic properties of the COSMO-optimized Fe1(IV)(di-μ-oxo)Fe2(IV) structure are also given in Table 1 (the last column outside the parentheses). In this structure, each iron has one short Fe−O distance (1.77 Å for Fe1−O1 and Fe2−O2), which was also reported for the MMOH-Q structure from EXAFS experiments.[98]

The COSMO-optimized structure of the Fe1(IV)(di-μ-oxo)Fe2(IV) cluster is by 6.6 kcal mol^{-1} (0.286 eV) lower in energy than the $S_{total} = 0$ state of the X(di-μ-oxo)-Trp48$^{\bullet+}$ structure. This energy gap is surprisingly large. The lower-energy Fe1(IV)(di-μ-oxo)Fe2(IV) state should be observable, unless there is a large kinetic barrier to attaining the diferryl state. In fact, reorganization energies of about 1 eV (23 kcal mol^{-1}) are quite common in biological electron transfer, so kinetics need not fully track the lowest-energy states. We notice that the Fe−Fe distance and most of the Fe−ligand distances in the optimized Fe1(IV)(di-μ-oxo)Fe2(IV) geometry are shorter than the corresponding ones in X(di-μ-oxo)-Trp48$^{\bullet+}$ structures. The earlier Fe(II)Fe(II) state of R2 has the longest Fe−Fe distance, 3.94 Å, of all known intermediates.[4] Upon O_2 binding and O−O bond breaking, the Fe−Fe distance should diminish and the first-shell ligands, especially the side chains of Asp84, His118, His241, and Glu204, should follow this decrease, in order to arrive at the Fe1(IV)(di-μ-oxo)Fe2(IV) state geometric minimum. Because the Fe−Fe distance of the X(di-μ-oxo)-Trp48$^{\bullet+}$ state is longer than that of Fe1(IV)(di-μ-oxo)Fe2(IV), the central diiron geometry on the reaction pathway should first arrive at a geometry similar to that of the X(di-μ-oxo)-Trp48$^{\bullet+}$ state. Then vertical electron transfer from Trp48 to Fe1 may happen at this stage. According to the Marcus theory, the crossing point(s) for electron transfer will occur at a geometry (geometries) intermediate to both X(di-μ-oxo)-Trp48$^{\bullet+}$ and Fe1(IV)(di-μ-oxo)Fe2(IV).

The α and β molecular orbital energy (eV) levels around HOMO and LUMO for the optimized Fe1(IV)(di-μ-oxo)Fe2(IV) cluster are shown in Figure 4. Simple one-electron orbital energy differences ($\varepsilon_i^{LUMO} - \varepsilon_j^{HOMO}$) do not represent the total excitation energies well because electron self-interaction energies in orbitals i and j are not included properly and electron relaxation effects upon excitation are not included either. Bearing this in mind, here we only qualitatively compare the energy gaps between the molecular orbitals of the optimized Fe1(IV)(di-μ-oxo)Fe2(IV) structure. In Figure 4, the sum of the atomic orbital contributions (which are larger than 1%) to the molecular orbital shows the location of the molecular orbital. Both α- and β-LUMOs mainly locate at site Fe1. Fe2 also has a large contribution to α-LUMO. Both α- and β-HOMOs are localized at the Trp48 side chain. The molecular orbital one-electron energy difference between α-HOMO and α-LUMO is only 1.3 kcal mol^{-1}, while β-HOMO and β-LUMO are degenerate. Therefore, it is very likely that the LUMOs and HOMOs exchange positions at some point (as mentioned above) when the central active site compresses to a geometry that is similar to that of the X(di-μ-oxo)-Trp48$^{\bullet+}$ state. In Figure 4, both α- and β-HOMO−3 orbitals localize at the Tyr122 side chain and are ~11 kcal mol^{-1} below the corresponding HOMOs, which also provides an explanation for why the "extra" electron comes from Trp48 and not Tyr122 in wild-type *E. coli* R2, even though Tyr122 is closer to the diiron center. As seen in the next section, this relative energy difference changes when Tyr122 deprotonates.

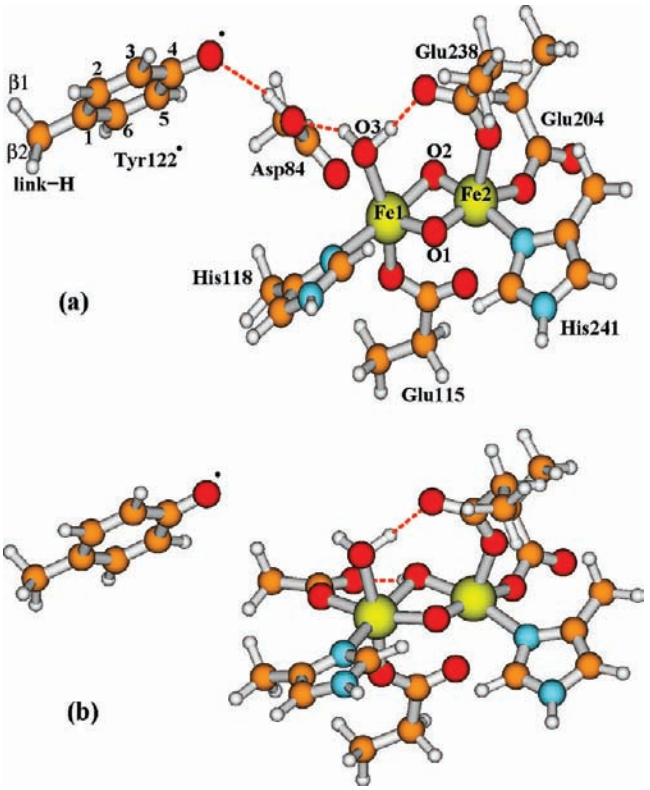

Figure 5. Active-site models for (a) X(di-μ-oxo)-Asp84H-Tyr122$^{\bullet}$ and (b) X(μ-oxo)(μ-hydroxo)-Tyr122$^{\bullet}$. The Asp84 side chain is protonated in model (a) but not in model (b). The outer-shell residue side chains shown in Figure 2, including Gln43, Trp48 (or Phe48), Trp111, Asp237, and water-621, are also included in calculations but not shown here.

Considering the oxidation process, where O_2 binds to Fe(II)Fe(II) and the subsequent reaction causes an overall compression, the "restraining" force or "steric strain" of the protein backbone may well increase the energy of the Fe1(IV)(di-μ-oxo)Fe2(IV) state. In our geometry optimizations described in section 3.1, only the linking hydrogen atoms on the second- and third-shell residue side chains were fixed. All atoms in the first-shell ligands were allowed to move. In order to test how the steric strain of the first-shell protein backbone will influence the structure and energy of the Fe1(IV)(di-μ-oxo)Fe2(IV) state, we started from the optimized X(di-μ-oxo)-Trp48$^{\bullet+}$ ($S_{total} = 0$) state geometry and fixed all linking hydrogen atoms according to this geometry and then optimized the rest of the atoms in the Fe1(IV)(di-μ-oxo)Fe2(IV) state. The main Fe−Fe and Fe−ligand distances and BS energy of this "more strained" Fe1(IV)(di-μ-oxo)Fe2(IV) state structure are also given in Table 1 (the last column in the parentheses). When the first-shell linking hydrogen atoms are also fixed according to the X(di-μ-oxo)-Trp48$^{\bullet+}$ ($S_{total} = 0$) state geometry, the Fe1(IV)(di-μ-oxo)Fe2(IV) state energy is increased by 2.7 kcal mol^{-1} (0.116 eV). This energy is expected to increase more if the strain is exerted according to the Fe(II)Fe(II) state geometry [or corresponding to the met Fe(III)Fe(III) state geometry, where the Fe−Fe distance is 3.42 Å, as observed in the X-ray crystal structure].[3] This may qualitatively explain that the formation rate constant of X-Trp48$^{\bullet+}$ is high (~200 s^{-1}),[11] and no accumulation of the diferryl state is observed even if O−O cleavage occurs before electron transfer from Trp48 to Fe1.

dx.doi.org/10.1021/ic1020127 |*Inorg. Chem.* 2011, 50, 2302–2320

Table 2. Calculated Fe−Fe and Fe−Ligand Distances (Å), NSPs of Fe1(III), Fe2(IV), and Tyr122•, BS State Energies E (eV), ^{57}Fe Mössbauer Isomer Shifts (δ, mm s^{-1}), Quadrupole Splittings (ΔE_Q, mm s^{-1}), and η and Proton Hyperfine Coupling Constants (A_{xx}, A_{yy}, and A_{zz}, MHz) for Tyr122• in Models X(di-μ-oxo)-Asp84H-Tyr122• and X(μ-oxo)(μ-hydroxo)-Tyr122• in Wild-Type and W48F Variant and Compared with Experimental (exp) Results

	wild-type		W48F		
	X(di-μ-oxo)-Asp84H-Tyr122•	X(μ-oxo)(μ-hydroxo)-Tyr122•	X(di-μ-oxo)-Asp84H-Tyr122•	X(μ-oxo)(μ-hydroxo)-Tyr122•	exp [a]
Fe1−Fe2	2.724	2.912	2.749	2.909	
Fe1−O1	1.860	1.928	1.877	1.928	
Fe2−O1	1.777	1.712	1.758	1.712	
Fe1−O2	1.942	2.049	1.949	2.046	
Fe2−O2	1.735	1.927	1.744	1.957	
Fe1−O3	2.097	2.191	2.119	2.174	
Fe1−N−His118	2.252	2.196	2.255	2.162	
Fe2−N−His241	2.145	2.153	2.143	2.169	
Fe1−O−Asp84	2.817	2.014	2.495	1.999	
Fe1−O−Glu115	1.963	1.975	1.973	2.006	
Fe2−O−Glu115	2.591	2.454	2.603	2.246	
Fe2−O−Glu204	1.957	1.914	1.961	1.916	
Fe2−O−Glu238	2.094	2.032	2.100	2.063	
NSP(Fe1)	4.01	4.07	4.02	4.07	
NSP(Fe2)	−3.23	−3.28	−3.24	−3.29	
NSP(C1-Tyr122•)	−0.39	−0.39	−0.39	−0.39	
NSP(C2-Tyr122•)	0.09	0.10	0.10	0.10	
NSP(C3-Tyr122•)	−0.22	−0.24	−0.22	−0.23	
NSP(C4-Tyr122•)	−0.05	−0.03	−0.04	−0.03	
NSP(O-Tyr122•)	−0.30	−0.31	−0.30	−0.31	
NSP(C5-Tyr122•)	−0.25	−0.25	−0.25	−0.26	
NSP(C6-Tyr122•)	0.10	0.10	0.10	0.11	
E	−880.5871	−880.7229	−849.8933	−850.0994	
δ(Fe1, Fe2)	(0.50, 0.22)	(0.51, 0.31)	(0.52, 0.21)	(0.51, 0.32)	(0.47, 0.22)
ΔE_Q(Fe1, Fe2)	(0.54, −0.33)	(−0.43, −0.64)	(0.46, −0.35)	(0.54, −0.59)	(−0.7, −0.64)
η(Fe1, Fe2)	(0.77, 0.66)	(0.53, 0.44)	(0.76, 0.80)	(0.88, 0.42)	(0.5, 2.7)
^{1}H(A_{xx}, A_{yy}, A_{zz}) for Tyr122•					
H-3	(23.9, 6.8, 19.4)	(25.1, 7.6, 20.0)	(24.2, 6.9, 19.6)	(24.6, 7.3, 19.7)	(26.9, 7.8, 19.6)
H-5	(26.1, 7.1, 21.0)	(26.3, 7.6, 21.3)	(26.2, 7.0, 21.0)	(27.2, 7.6, 21.9)	(26.9, 7.8, 19.6)
H-β1	−(69.6, 62.9, 64.5)	−(80.9, 74.2, 75.9)	−(73.2, 66.6, 68.1)	−(69.5, 63.1, 64.6)	(57.8, 52.1, 54.9)
H-2	−(6.4, 0.7, 3.1)	−(6.7, 1.2, 3.5)	−(6.5, 0.8, 3.9)	−(6.8, 1.2, 3.5)	∼(0, 0, 0)
H-6	−(6.5, 0.6, 3.0)	−(6.8, 1.0, 3.5)	−(6.6, 0.6, 3.1)	−(7.0, 1.2, 3.7)	∼(0, 0, 0)
H-β2	(−3.8, 1.3, 0.9)	−(11.6, 6.0, 6.9)	(−4.8. −0.09, 0.4)	(−4.4, 0.3, 0.9)	∼ (0, 0, 0)
H-link	−(57.4, 50.5, 52.0)	−(36.5, 30.5, 31.7)	−(52.8, 46.1, 47.6)	−(53.9, 47.3, 48.8)	

[a] Experimental data are for W48F mutant *E. coli* R2, taken from ref 12.

When the geometries between the two optimized Fe1(IV)(di-μ-oxo)Fe2(IV) state structures (data outside and inside the parentheses of the last column of Table 1) are compared, the significant Fe−ligand distance changes are for Fe1−O−Asp84, Fe1−N−His118, and Fe2−N−His241, which lengthen by 0.04, 0.03, and 0.05 Å, respectively, when the linking hydrogen atoms are fixed on Asp84, His118, and His241 side chains. Asp84 has a shorter and therefore more stiff side chain compared with Glu side chains, and it is the only difference between the first-shell structures of RNR-R2 and MMOH active sites. In MMOH, the site where Asp84 sits in R2 is also a Glu.[94] It is likely that the strain of Asp84 is another reason why accumulation of the Fe1(IV)(di-μ-oxo)Fe2(IV) state in *E. coli* R2 is prevented. Later we will see that the Fe−O−Asp84 bond breaks when the proton from Tyr122 transfers to Asp84 in the X(di-μ-oxo)-Tyr122• structure.

4.2. Calculated Properties of Models X(di-μ-oxo)-Asp84H-Tyr122• and X(μ-oxo)(μ-hydroxo)-Tyr122•. In the absence of a reductant near Trp48$^{\bullet+}$, Tyr122 will then donate an electron to Trp48$^{\bullet+}$, and the X-Tyr122• diradical will be formed.[11,12] Because Tyr122• is found in the neutral deprotonated form, electron transfer from Tyr122 to Trp48$^{\bullet+}$ is coupled with proton transfer, and proton transfer may even happen prior to electron transfer. The direct proton acceptor of this proton transfer would be the carboxylate group of Asp84, which has a hydrogen-bonding interaction with the −OH group of Tyr122 in

dx.doi.org/10.1021/ic1020127 |*Inorg. Chem.* 2011, 50, 2302–2320

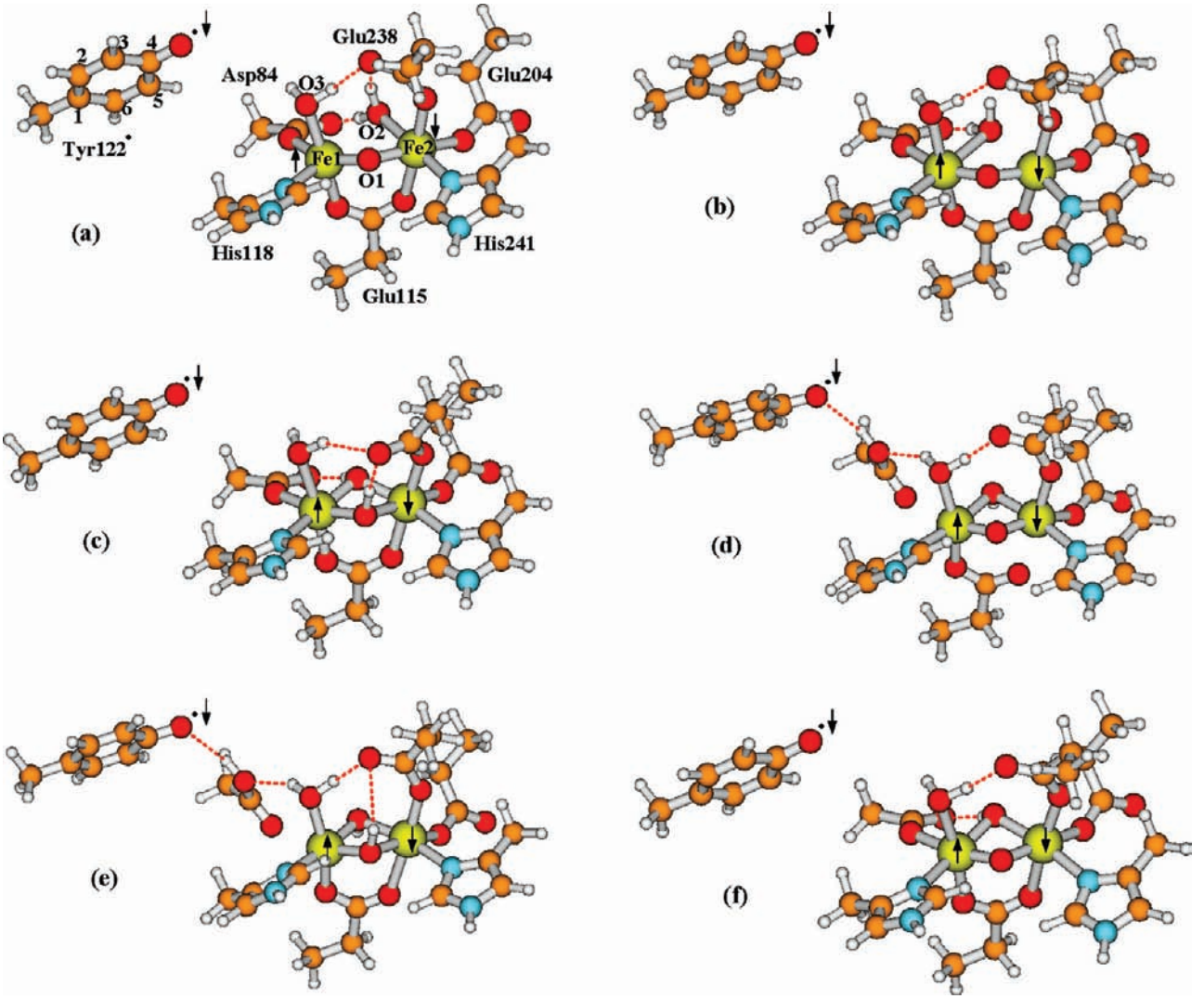

Figure 6. Active-site models for the active (A) state Fe1(III)Fe2(III)-Tyr122• of *E. coli* R2 studied in the current paper. The following names are given for these models and discussed in the text: (a) A(O_{br},H_2O_{t2}); (b) A(O_{br},H_2O_{t1}); (c) A(OH^-_{br},OH^-_{br}); (d) A(O_{br},OH^-_{br})-Asp84H; (e) A(OH^-_{br},OH^-_{br})-Asp84H; (f) A(O_{br},OH^-_{br}), where "br" means the oxygen species is in the "bridging" position between Fe1 and Fe2, "t2" and "t1" in models a and b represent the ligand water molecule at site O2 "terminally" binding to Fe2 and Fe1, respectively, and Asp84H means that the side chain of Asp84 is protonated in that model. The arrows indicate the directions of the net spins on Fe1, Fe2, and Tyr122•. The outer-shell residue side chains shown in Figure 2, including Gln43, Trp48, Trp111, Asp237, and water-621, are also included in the calculations but not shown here.

X-Trp48$^{\bullet+}$. Starting from the optimized S_{total} = 0 state X(di-μ-oxo)-Trp48$^{\bullet+}$ structure, we simply moved the proton from Tyr122 to Asp84 and optimized the geometry with the same charge and spin state as X(di-μ-oxo)-Asp84H-Trp48$^{\bullet+}$. During optimization, the proton stayed on Asp84 and hydrogen-bonded to the oxygen atom of Tyr122, the Fe1−O(Asp84) bond was gradually elongated and was finally broken at a distance 2.817 Å, and, importantly, the X-Tyr122• state was automatically obtained. The center of the optimized X(di-μ-oxo)-Asp84H-Tyr122• model is shown in Figure 5a, and the main calculated properties of this model are given in Table 2. The total net spin on the carbon and oxygen atoms of the Tyr122 ring is −1 (spin down), definitely showing the Tyr122• radical state.

If Trp48$^{\bullet+}$ is reduced by a nearby reductant, then X alone will oxidize Tyr122 to Tyr122•, with a slower rate (0.85 ± 0.15 s^{-1}) than the oxidation by X-Trp48$^{\bullet+}$ (6.2 ± 1.2 s^{-1}).[11] Siegbahn studied the pathway of X → Fe(III)Fe(III)-Tyr122• and proposed that a water molecule goes between Tyr122 and Asp84 (and also hydrogen bonds with the terminal H_2O ligand) in X as a bridge for proton transfer from Tyr122 to Asp84.[23] A water molecule between Tyr and Asp is commonly observed in class Ib RNRs, where Tyr and Asp are far from each other.[102] However, no such water molecule has ever been observed between Tyr122 and Asp84 in class Ia *E. coli* R2 crystal structures, including the iron-free form.[103] We therefore did not have such a water molecule in the X-Trp48$^{\bullet+}$ → X-Tyr122• pathway.

Experimentally, ^{57}Fe Mössbauer isomer shifts (δ) and quadrupole splittings (ΔE_Q) for X and the proton hyperfine coupling constants (A_{xx}, A_{yy}, and A_{zz}) for Tyr122• were determined for the X-Tyr122• diradical state in mutant W48F *E. coli* R2.[12] Our calculated properties are compared with the experimental data in Table 2. For the current X(di-μ-oxo)-Asp84H-Tyr122• model, the calculated δ(Fe1, Fe2) = (0.50, 0.22 mm s^{-1}) are highly consistent with the observed values (0.47, 0.22 mm s^{-1}). The

dx.doi.org/10.1021/ic1020127 |*Inorg. Chem.* 2011, 50, 2302–2320

Table 3. Calculated Fe−Fe and Fe−Ligand Distances (Å), NSPs of Fe1(III), Fe2(III), and Tyr122•, BS State Energies E (eV), ^{57}Fe Mössbauer Isomer Shifts (δ, mm s^{-1}), Quadrupole Splittings (ΔE_Q, mm s^{-1}), and η Values for the Fe1(III)Fe2(III)-Tyr122• Active-Site Models[a]

	(a) A(O_{br}-H_2O_{t2})	(b) A(O_{br}-H_2O_{t1})	(c) A(OH^-_{br}-OH^-_{br})	(d) A(O_{br}-OH^-_{br})-Asp84H	(e) A(OH^-_{br}-OH^-_{br})-Asp84H	(f) A(O_{br}-OH^-_{br})	exp [b]
Fe1−Fe2	3.151	3.131	3.053	2.881	3.079	2.889	
Fe1−O1	1.782	1.795	1.959	1.781	1.933	1.785	
Fe2−O1	1.826	1.818	2.046	1.848	2.159	1.847	
Fe1−O2	2.744	2.412	2.003	2.084	1.993	2.016	
Fe2−O2	2.278	2.506	2.023	2.111	2.081	2.075	
Fe1−O3	2.215	2.196	2.345	2.129	2.103	2.248	
Fe1−N−His118	2.123	2.152	2.238	2.207	2.148	2.276	
Fe2−N−His241	2.206	2.150	2.220	2.238	2.167	2.239	
Fe1−O−Asp84	2.041	2.090	2.011	3.032	2.962	2.065	
Fe1−O−Glu115	1.995	2.006	2.001	1.975	1.946	2.033	
Fe2−O−Glu115	2.245	2.165	2.153	2.427	2.224	2.271	
Fe2−O−Glu204	2.014	2.013	1.966	2.023	1.916	2.066	
Fe2−O−Glu238	2.042	2.037	2.060	2.032	1.994	2.060	
NSP(Fe1)	4.05	4.04	4.16	4.02	4.20	3.85	
NSP(Fe2)	−4.05	−4.04	−4.14	−4.06	−4.13	−4.04	
NSP(C1-Tyr122•)	−0.39	−0.39	−0.39	−0.38	−0.39	−0.29	
NSP(C2-Tyr122•)	0.10	0.10	0.10	0.09	0.09	0.08	
NSP(C3-Tyr122•)	−0.24	−0.24	−0.24	−0.22	−0.22	−0.18	
NSP(C4-Tyr122•)	−0.03	−0.03	−0.03	−0.04	−0.05	−0.02	
NSP(O-Tyr122•)	−0.31	−0.31	−0.31	−0.30	−0.30	−0.25	
NSP(C5-Tyr122•)	−0.25	−0.25	−0.25	−0.24	−0.25	−0.19	
NSP(C6-Tyr122•)	0.10	0.10	0.10	0.10	0.10	0.08	
E	−885.6346	−885.7093	−885.5971	−885.2601	−884.7301	−885.3473	
δ(Fe1, Fe2)	(0.47, 0.54)	(0.50, 0.53)	(0.48, 0.53)	(0.48, 0.54)	(0.50, 0.54)	(0.44, 0.56)	(0.45, 0.55)
ΔE_Q(Fe1, Fe2)	(−1.72, −1.78)	(−1.63, −1.70)	(0.98, 0.64)	(−0.64, −1.46)	(2.50, 0.65)	(−1.06, −1.30)	(−2.44, −1.62)
η(Fe1, Fe2)	(0.44, 0.14)	(0.38, 0.26)	(0.53, 0.82)	(0.71, 0.63)	(0.54, 0.51)	(0.36, 0.56)	(0.2, 0.6)
pK_a [c]							
(e) → (d) + H$^+$					1.27		
(a) → (f) + H$^+$	15.03						
(b) → (f) + H$^+$		16.29					
(c) → (f) + H$^+$			14.40				

[a] The diiron centers of these models are shown in Figure 6a−f. [b] Taken from ref 105. [c] Calculated according to eq 5, with the relevant BS state energies given in this table.

absolute values of the ΔE_Q's are also reasonably reproduced. Our previous calculations show that the correct sign of ΔE_Q is difficult to predict when η is close to 1. The sign of the calculated ΔE_Q can vary with the chosen computational methods, atomic basis sets, dielectric constant of the environment, different model structures, and size of the quantum cluster.[31] The standard deviation (SD) of ΔE_Q for the OPBE potential on the test set of synthetic complexes is 0.25 mm s^{-1},[54] so the absolute values of our calculated ΔE_Q here (0.54, 0.33 mm s^{-1}) are about 1 SD from experiment (0.7, 0.64 mm s^{-1}).

From the ADF output, we extracted the local Tyr122• ^{1}H hyperfine **A** tensors corresponding to Tyr radical spin $S_1 = {}^1/_2$ and the spin Hamiltonian term $[\sum_i \mathbf{S}_1 \cdot \mathbf{A}_i \cdot (\mathbf{I}_H)_i]$.[12] We cross-checked that these $\mathbf{A}_i$ are the same when computed for either $S_{total} = 1$ or $S_{total} = 0$. (It also turned out that the energies of the $S_{total} = 1$ and $S_{total} = 0$ states are almost the same.) The calculated ^{1}H hyperfine **A** tensors for H-3 and H-5 of Tyr122• (see Figure 5a for notations) are very similar and agree very well with the corresponding experimental values. One of the calculated β protons ($H_{\beta 1}$) has a large **A** tensor (>50 MHz), as observed in experiment. Experimentally, the hyperfine couplings for protons H-2, H-6, and the other H-β were very weak and were not reported.[12] Correspondingly, our calculated **A** tensors for these protons are also small.

We recall that, in the met Fe(III)Fe(III) *E. coli* R2 crystal structure (see $R2_{ox(met)}$ in Figure 1) (PDB code: 1RIB),[3] the bridging site O2 changes to a terminally bound water molecule, which hydrogen bonds with the carboxylate group of Asp84. Therefore, another possible conformation for the X-Tyr122• state would have the protonated Asp84 side chain in the X(di-μ-oxo)-Asp84H-Tyr122• model (Figure 5a) rotating and donating the proton to site O2. See Figure 5b for this new structure, which is named X(μ-oxo)(μ-hydroxo)-Tyr122• hereafter. The calculated properties of this model are also given in Table 2.

When site O2 is protonated, the central geometry of the model X(μ-oxo)(μ-hydroxo)-Tyr122• is different from that of X(di-μ-oxo)-Asp84H-Tyr122•. The Fe−Fe and Fe−O2 distances are much longer in X(μ-oxo)(μ-hydroxo)-Tyr122•, resulting in different Mössbauer properties. The predicted quadrupole-splitting values still do not agree well with experiment. The calculated δ(Fe1) = 0.51 mm s^{-1} for X(μ-oxo)(μ-hydroxo)-Tyr122• is similar to that (0.50 mm s^{-1}) for X(di-μ-oxo)-Asp84H-Tyr122• and is close to the observed value of 0.47 mm s^{-1}. However, the predicted δ(Fe2) = 0.31 mm s^{-1} for X(μ-oxo)(μ-hydroxo)-Tyr122• is larger (by 0.09 mm s^{-1}) than that for X(di-μ-oxo)-Asp84H-Tyr122• and the experimental value (both are 0.22 mm s^{-1}). Therefore, the calculated Mössbauer isomer shifts for model X(di-μ-oxo)-Asp84H-Tyr122• are closer to experimental results than those for model X(μ-oxo)(μ-hydroxo)-Tyr122•. On the other hand, the BS state electronic energy of X(μ-oxo)(μ-hydroxo)-Tyr122• is by 3 kcal mol^{-1} lower than that of X(di-μ-oxo)-Asp84H-Tyr122•. However, considering the accuracy of

dx.doi.org/10.1021/ic1020127 |*Inorg. Chem.* 2011, 50, 2302–2320

DFT and solvation calculations, this is not a large energy difference. The change of the active-site structure from the isomer X(di-μ-oxo)-Asp84H-Tyr122$^{\bullet}$ (where Asp84 is protonated) to X(μ-oxo)(μ-hydroxo)-Tyr122$^{\bullet}$ will be determined by the rotational potential energy barrier of the protonated Asp84 side chain and a potential energy barrier for Asp84(O)-Fe1 rebinding and Asp84(OH) to O2 proton transfer. The calculated hyperfine **A** tensors for H-3 and H-5 of Tyr122$^{\bullet}$ in X(μ-oxo)-(μ-hydroxo)-Tyr122$^{\bullet}$ are essentially the same as those in X(di-μ-oxo)-Asp84H-Tyr122$^{\bullet}$.

We note that the ^{57}Fe Mössbauer and ^{1}H-Tyr122$^{\bullet}$ hyperfine experimental data were obtained for the W48F mutant R2, while our calculations so far were performed on the wild-type X-Tyr122$^{\bullet}$ cluster models. In order to see if the mutation will influence the calculated properties, we changed the Trp48 side chain to the Phe48 side chain (assuming that the C_{α} and C_{β} positions of Trp48 and Phe48 are the same) in both X(di-μ-oxo)-Asp84H-Tyr122$^{\bullet}$ and X(μ-oxo)(μ-hydroxo)-Tyr122$^{\bullet}$ models. The geometries of the W48F models were also optimized in COSMO. The calculated properties are also given in Table 2 for comparison. Overall, the properties of the mutant models are very similar to those of the corresponding wild-type models. Still, the predicted δ(Fe2) = 0.21 mm s^{-1} in the W48F-X(di-μ-oxo)-Asp84H-Tyr122$^{\bullet}$ model reproduces the observed value of 0.22 mm s^{-1} very well, and δ(Fe2) in the W48F-X(μ-oxo)(μ-hydroxo)-Tyr122$^{\bullet}$ model is too large (0.32 mm s^{-1}). Therefore, the X(di-μ-oxo)-Asp84H-Tyr122$^{\bullet}$ model is more likely to represent the X-Tyr122$^{\bullet}$ active-site structure.

4.3. Feasible Active-Site Conformations in the Fe1(III)Fe2-(III)-Tyr122$^{\bullet}$ Active State of *E. coli* R2. The active state of Fe1(III)Fe2(III)-Tyr122$^{\bullet}$ is formed by electron transfer to the X-Tyr122$^{\bullet}$ center or by Tyr122 being oxidized by X. The complex can also pick up a proton as well. As far as we know, no X-ray crystal structure is available for the active state of R2. ^{57}Fe Mössbauer spectra for the active state of R2 were first reported over 30 years ago[104] and later were redone and checked by Que's group.[105] Mössbauer, ^{1}H NMR, optical, and resonance Raman experiments show that the major spectroscopic properties of the active site do not change when the tyrosyl radical is reduced,[104−106] indicating similar structures of the active and inactive (met) diferric center of R2. On the basis of the met Fe1(III)Fe2(III) crystal structure ($R2_{ox(met)}$ in Figure 1) and the X-Tyr122$^{\bullet}$ models studied above, we constructed six active-site models for the active form of R2, in order to investigate the feasible conformations of R2 in the active state by comparing the relative energies of these model clusters and their calculated Mössbauer properties with experiments.

The diiron centers of the six active state model clusters are shown in Figure 6a−f. The names of these models are given as follows:

(a) A(O_{br},H_2O_{t2}) (Figure 6a), where "A" represents the active Fe1(III)Fe2(III)-Tyr122$^{\bullet}$ state, O_{br} is the bridging (br) oxo at site O1, H_2O_{t2} represents the H_2O at site O2, and t2 means terminal binding to Fe2. This structure is basically the same as that of the met diferric ($R2_{ox(met)}$ in Figure 1) form, as seen in the X-ray crystal structure, but with the neutral deprotonated Tyr122$^{\bullet}$. Starting from the X(di-μ-oxo)-Tyr122$^{\bullet}$ state (Figure 5a), A(O_{br},H_2O_t) may be formed by the following process: first, an electron has to transfer to Fe2(IV), then the protonated Asp84 side chain rotates to donate the proton to O2 (see Figure 5b), and meanwhile another proton also needs to transfer to O2. Site O2 then becomes a water molecule, which hydrogen bonds to the Asp84 side chain. The Fe1−O2 distance elongates and the H_2O terminally binds only to Fe2(III). This process is similar to the X → Fe(III)Fe-(III)-Tyr122$^{\bullet}$ pathway proposed by Siegbahn with smaller models.[23] The main difference is that, in Siegbahn's model, a water molecule is inserted between Tyr122 and Asp84, X is in Fe1(IV)Fe2(III) state rather than the Fe1(III)Fe2(IV) state, and the bridging O2 site in X is a hydroxo rather than a μ-oxo.

(b) A(O_{br},H_2O_{t1}) (Figure 6b). The difference between this model and A(O_{br},H_2O_{t2}) is the position of the H_2O at site O2. The initial purpose for studying this model is to test if the water molecule at site O2 would stay in the bridging (br) position between Fe1(III) and Fe2(III) like the bridging hydroxo in Figure 5b. However, after geometry optimization, the Fe2−O2 bond breaks. Therefore, the H_2O at site O2 terminally binds to Fe1 (t1). Alternatively, this complex can be considered a weak bridging structure with the H_2O bridge between Fe1 and Fe2.

(c) A(OH^{-}_{br},OH^{-}_{br}) (Figure 6c). Although the ligand residue side chains in the diiron centers of *E. coli* R2 and MMOH are very similar, their X-ray crystal structures for both Fe(II)Fe(II) and Fe(III)Fe(III) states are different. The Fe(III)Fe(III) state of MMOH contains two μ-OH^{-} species[94] rather than the one μ-oxo and one H_2O_t in met diferric R2. The model A(OH^{-}_{br},OH^{-}_{br}) is constructed in order to see whether the active form of R2 would favor the di-μ-OH^{-} structure energetically.

(d) A(O_{br},OH^{-}_{br})-Asp84H (Figure 6d). This model is constructed to see if the protonated Asp84 in the active state will stay in the position as in X(di-μ-oxo)-Tyr122$^{\bullet}$ (Figure 5a), and site O2 becomes protonated μ-OH^{-}.

(e) A(OH^{-}_{br},OH^{-}_{br})-Asp84H (Figure 6e). Compared with A(O_{br},OH^{-}_{br})-Asp84H, site O1 is also protonated and becomes a μ-OH^{-} in this model.

(f) A(O_{br},OH^{-}_{br}) (Figure 6f). This structure is evaluated to see if it is possible that the active form stays in a protonation state analogous to that of the X(μ-oxo)(μ-hydroxo)-Tyr122$^{\bullet}$ structure (Figure 5b). Even if not, later when we calculate the redox potential for X(di-μ-oxo)-Tyr122$^{\bullet}$ + H^{+} + e^{-} → active form, we will also need the energy of this structure. This structure is similar to that in Figure 5b but with binding at Fe2−O−Glu115, making Glu115 bidentate to Fe1 and Fe2.

All geometries of these models were optimized within COSMO according to section 3.1. The main Fe−ligand distances, NSPs on Fe1(III), Fe2(III), and Tyr122$^{\bullet}$, BS state energies after geometry optimizations, and calculated and experimental ^{57}Fe Mössbauer properties are given in Table 3.

The calculated NSPs for all six models are nearly the same. All are clearly in the Fe1(III)↑-Fe2(III)↓-Tyr122$^{\bullet}$↓ state (the arrows represent the net spins up or down). It is reasonable to see that, with a terminally bound H_2O to Fe2 (Figure 6a), the model A(O_{br},H_2O_{t2}) yields the longest Fe1−Fe2 distance. In model A(O_{br},H_2O_{t1}) (Figure 6b), the H_2O at site O2 is actually far from Fe1 (2.412 Å) but even farther from Fe2 (2.506 Å). This model turned out to have the lowest BS state energy among the first four models (a−d), which have the same number of atoms. Models a−d are tautomeric states, so their energies can be directly compared.

Model A(O_{br},OH^-_{br})-Asp84H (Figure 6d) has the highest energy of models a−d, which is 10.4 kcal mol^{-1} higher than that of A(O_{br},H_2O_{t1}). Because this is a comparatively large energy difference, the model A(O_{br},OH^-_{br})-Asp84H is probably not the ground-state structure of *E. coli* R2 in the Fe1(III)Fe2(III)-Tyr122$^\bullet$ active state. Model A(OH^-_{br},OH^-_{br}) (Figure 6c) also has higher energy than A(O_{br},H_2O_{t1}), by 2.6 kcal mol^{-1}. According to this energy difference alone, one cannot rule out this active-site structure. However, because the X-ray crystal structure for met diferric R2 shows the active site in (O_{br},H_2O_{t2}) form, the active state of R2 may not stay in the (OH^-_{br},OH^-_{br}) conformation either. The next model A(O_{br},H_2O_{t2}) (Figure 6a), which was constructed according to the met diferric R2 crystal structure, is only 1.7 kcal mol^{-1} higher in energy than A(O_{br},H_2O_{t1}). Considering the very similar conformations of A(O_{br},H_2O_{t2}) and A(O_{br},H_2O_{t1}), both structures may represent the active site of the active state R2, meaning that the H_2O ligand at site O2 either binds to Fe1 or Fe2 or is in a bridging position because of the shallow potential energy surface.

Model A(OH^-_{br},OH^-_{br})-Asp84H (Figure 6e) has one more proton than the first four models (a−d). For comparing the energetic stability between this model and A(O_{br},OH^-_{br})-Asp84H (Figure 6d), we calculated the pK_a for the process A(OH^-_{br},OH^-_{br})-Asp84H → A(O_{br},OH^-_{br})-Asp84H + H^+ according to eq 5 by replacing E[X(di-μ-oxo)-Trp48$^{\bullet+}$] and E[X(μ-oxo)(μ-hydroxo)-Trp48$^{\bullet+}$ with E[A(O_{br},OH^-_{br})-Asp84H] and E[A(OH^-_{br},OH^-_{br})-Asp84H], respectively, and obtained the value 1.27. Therefore, the A(O_{br},OH^-_{br})-Asp84H structure is energetically more stable than A(OH^-_{br},OH^-_{br})-Asp84H. Because A(O_{br},OH^-_{br})-Asp84H has substantially higher energy than A(O_{br},H_2O_{t1}) and A(O_{br},H_2O_{t2}), A(OH^-_{br},OH^-_{br})-Asp84H is ruled out for the active state structure of *E. coli* R2.

By contrast, model A(O_{br},OH^-_{br}) (Figure 6f) has one less proton than the first four models (a−d). In a similar way, we also calculated the pK_a's for the processes

$$A(O_{br}, H_2O_{t2}) \rightarrow A(O_{br}, OH^-_{br}) + H^+ \quad (6)$$

$$A(O_{br}, H_2O_{t1}) \rightarrow A(O_{br}, OH^-_{br}) + H^+ \quad (7)$$

$$A(OH^-_{br}, OH^-_{br}) \rightarrow A(O_{br}, OH^-_{br}) + H^+ \quad (8)$$

and obtained pK_a values of 15.0, 16.3, and 14.4, respectively. Therefore, energetically model A(O_{br},OH^-_{br}) (Figure 6f) is also far less stable than models a−c and about 2.4 kcal mol^{-1} less stable than model d at pH 7 (equivalently, the calculated pK_a for Asp84H in model d is 8.7, assuming the same ΔZPE given in eq 5).

The calculated Mössbauer isomer shifts for the six active state models (in Table 3) are very consistent with the experiment. Models a, c, d, and f almost exactly reproduce the observed δ values. However, the predicted Mössbauer quadrupole splittings for models c, d, and f are far from the experimental results. The very large observed $|\Delta E_Q(Fe1)|$ = 2.44 mm s^{-1} is only reproduced by model e (2.50 mm s^{-1}). However, the calculated $|\Delta E_Q(Fe2)|$ = 0.65 mm s^{-1} for model e is too small compared with the experiment (1.62 mm s^{-1}). Models a and b yield very similar quadrupole splittings. Although the calculated $|\Delta E_Q(Fe1)|$ values for models a and b are not as large as 2.44 mm s^{-1}, both predicted $|\Delta E_Q(Fe1)|$ and $|\Delta E_Q(Fe2)|$ values are relatively large and closer to the experiment than other models.

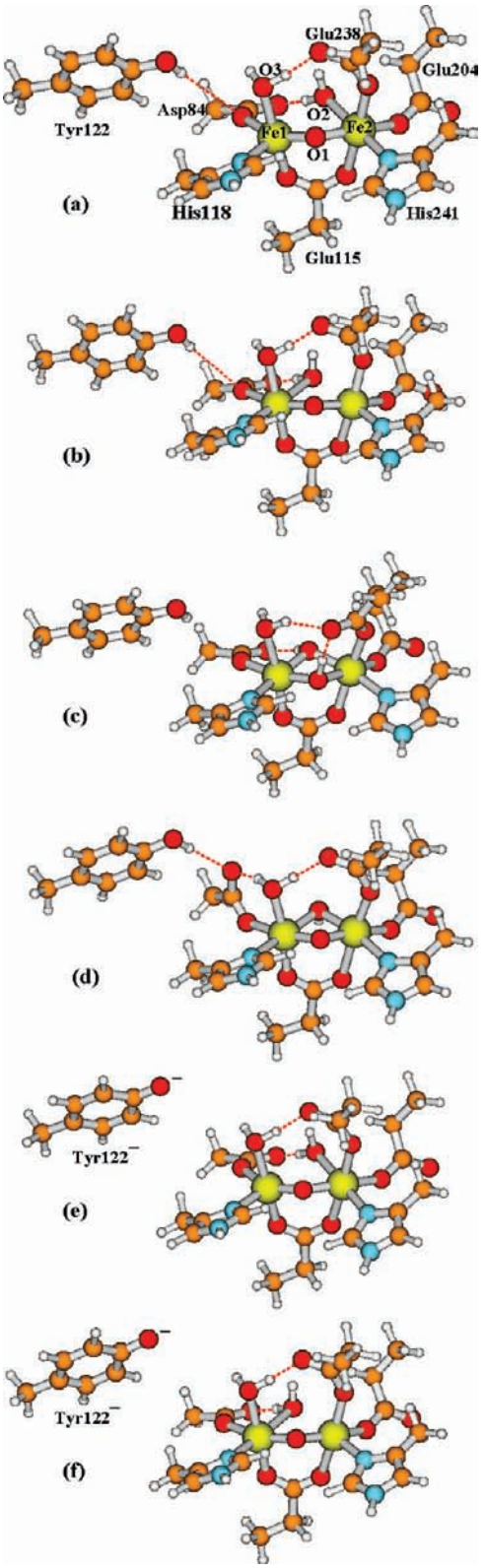

Figure 7. Active-site models for the met (M) diferric Fe1(III)Fe2(III) state of *E. coli* R2 studied in the current paper. The following names are given for these models and discussed in the text: (a) M(O_{br},H_2O_{t2}); (b) M(O_{br},H_2O_{t1}); (c) M(OH^-_{br},OH^-_{br}); (d) M(O_{br},OH^-_{br}); (e) M(O_{br},H_2O_{t2})-Tyr122$^-$; (f) M(O_{br},H_2O_{t1})-Tyr122$^-$. The outer-shell residue side chains shown in Figure 2, including Gln43, Trp48, Trp111, Asp237, and water-621, are also included in the calculations but not shown here.

dx.doi.org/10.1021/ic1020127 |*Inorg. Chem.* 2011, 50, 2302–2320

Table 4. Calculated Fe−Fe and Fe−Ligand Distances (Å), Fe NSPs, BS State Energies E (eV), ^{57}Fe Mössbauer Isomer Shifts (δ, mm s^{-1}), Quadrupole Splittings (ΔE_Q, mm s^{-1}), and η Values for the Met (M) Diferric Fe1(III)Fe2(III) Active-Site Models[a]

	(a) M(O_{br},-H_2O_{t2})	(b) M(O_{br},-H_2O_{t1})	(c) M(OH^-_{br},-OH^-_{br})	(d) M(O_{br},-OH^-_{br})	(e) M(O_{br},-H_2O_{t2})-$Tyr122^-$	(f) M(O_{br},-H_2O_{t1})-$Tyr122^-$	exp [b]
Fe1−Fe2	3.192	3.141	3.052	2.919	3.176	3.137	3.422
Fe1−O1	1.786	1.798	1.960	1.806	1.783	1.798	2.170
Fe2−O1	1.822	1.814	2.043	1.815	1.825	1.815	2.060
Fe1−O2	2.819	2.382	1.999	2.151	2.808	2.405	3.105
Fe2−O2	2.372	2.585	2.027	2.090	2.329	2.550	2.264
Fe1−O3	2.204	2.181	2.340	2.162	2.220	2.190	2.109
Fe1−N−His118	2.120	2.171	2.241	2.265	2.119	2.161	2.146
Fe2−N−His241	2.182	2.148	2.220	2.280	2.190	2.150	2.292
Fe1−O−Asp84	2.064	2.135	2.029	2.132	2.036	2.090	2.159
Fe1−O−Glu115	1.990	2.001	1.999	2.029	1.997	2.006	1.829
Fe2−O−Glu115	2.205	2.157	2.150	2.333	2.234	2.161	1.951
Fe2−O−Glu204	2.015	2.005	1.964	2.092	2.016	2.012	2.122
Fe2−O−Glu238	2.029	2.028	2.066	2.042	2.030	2.030	2.119
NSP(Fe1)	4.05	4.03	4.16	4.02	4.05	4.04	
NSP(Fe2)	−4.05	−4.03	−4.14	−4.02	−4.05	−4.04	
E	−890.4791	−890.5096	−890.3996	−890.2911	−890.0441	−890.0860	
δ(Fe1, Fe2)	(0.48, 0.54)	(0.51, 0.52)	(0.48, 0.53)	(0.50, 0.53)	(0.47, 0.54)	(0.50, 0.52)	(0.45, 0.55)
ΔE_Q(Fe1, Fe2)	(−1.68, −1.69)	(−1.53, −1.70)	(0.92, 0.66)	(−1.32, −1.48)	(−1.70, −1.72)	(−1.63, −1.73)	(−2.44, −1.62)
η(Fe1, Fe2)	(0.51, 0.22)	(0.45, 0.28)	(0.44, 0.85)	(0.25, 0.57)	(0.43, 0.17)	(0.39, 0.30)	(0.2, 0.6)
pK_a[c]							
(a) → (d) + H^+	13.36						
(b) → (d) + H^+		13.87					
(a) → (e) + H^+	16.98 [d]						
(b) → (f) + H^+		16.78 [d]					

[a] The diiron centers of these models are shown in Figure 7a−f. [b] Geometry is taken from chain A of the met diferric crystal structure (PDB code: 1RIB, resolution 2.2 Å),[3] and the Mössbauer data are taken from ref 105. [c] Calculated according to eq 5, with the relevant BS state energies given in this table. [d] ΔZPE = −8.03 kcal mol^{-1} is used here, obtained from frequency calculations for the neutral Tyr122 and deprotonated $Tyr122^-$ side chains. The reaction processes are also written in eqs 13b and 14b.

Therefore, based on the calculated energetic and Mössbauer properties, models a and b are the best among the six models in representing the ground-state structure of *E. coli* R2 in the Fe1(III)Fe2(III)-$Tyr122^•$ active state. Model (d) A(O_{br},OH^-_{br})-Asp84H (Figure 6d), having higher energy than models a and b, is a likely intermediate for the radical (hole) transfer pathway from subunit R2 to R1 because the close proximity of the proton on Asp84H to $Tyr122^•$ will facilitate the coupled e^-/H^+ reduction of $Tyr122^•$, with a transient hole then appearing on $Trp48^{•+}$.

4.4. Met Diferric Fe1(III)Fe2(III) Active-Site Structures. We already know that the X-ray crystal structure shows the (O_{br}, H_2O_{t2})-type active site for the met diferric active site. Our calculations in the section above show that the active state model A(O_{br},H_2O_{t1}) (Figure 6b) is a little lower and model A(OH^-_{br}, OH^-_{br}) (Figure 6c) is higher in energy than model A(O_{br}, H_2O_{t2}) (Figure 6a). In this section, we will examine the relative energies from OPBE calculations for these three structures in the met diferric Fe1(III)Fe2(III) state. Adding a hydrogen atom to $Tyr122^•$ in models A(O_{br},H_2O_{t2}), A(O_{br},H_2O_{t1}), and A(OH^-_{br}, OH^-_{br}), we obtained the initial geometries for the corresponding met (M) diferric Fe1(III)Fe2(III) state models M(O_{br}, H_2O_{t2}), M(O_{br},H_2O_{t1}), and M(OH^-_{br},OH^-_{br}). These structures were then optimized as described in section 3.1 and are shown in Figure 7a−c, respectively. The calculated geometric and Mössbauer properties are given in Table 4 and compared with the experimental results.

The main calculated Fe−ligand distances, calculated isomer shifts, and quadrupole splittings of models M(O_{br},H_2O_{t2}), M(O_{br}, H_2O_{t1}), and M(OH^-_{br},OH^-_{br}) are very similar to the corresponding values for A(O_{br},H_2O_{t2}), A(O_{br},H_2O_{t1}), and A(OH^-_{br}, OH^-_{br}), respectively. This further supports the experimental demonstration that the $Tyr122^•$ radical has very little effect on Mössbauer spectra of ^{57}Fe in R2[104] and that the active-site geometries of the active form and the met diferric form are very similar.

The BS state energy of model M(OH^-_{br},OH^-_{br}) is still higher than those of M(O_{br},H_2O_{t2}) and M(O_{br},H_2O_{t1}). Therefore, as observed in the crystal structure, the met diferric center is not in the (OH^-_{br},OH^-_{br}) form. The calculated BS energies of models M(O_{br},H_2O_{t2}) and M(O_{br},H_2O_{t1}) are almost degenerate (the difference is only 0.7 kcal mol^{-1}). From an energetic point of view, both M(O_{br},H_2O_{t2}) and M(O_{br},H_2O_{t1}) may coexist. Because the calculated isomer shifts of M(O_{br},H_2O_{t2}) are closer to the experiment than M(O_{br},H_2O_{t1}), it is also possible that the met diferric active site only exists in the M(O_{br},H_2O_{t2}) form, depending on the detailed structural changes during the $Tyr122^•$ radical reduction and proton-transfer processes.

In Figure 7d and column d of Table 4, we present another met diferric model, M(O_{br},OH^-_{br}), which contains a μ-oxo bridge at site O1 and a μ-hydroxo bridge at site O2. This model has one proton less than the met models a−c mentioned previously. Considering the catalytic cycle of radical transfer starting from the transient intermediate state A(O_{br},OH^-_{br})-Asp84H (Figure 6d) by electron transfer (from Trp48) and proton transfer from Asp84H to $Tyr122^•$, M(O_{br},OH^-_{br}) is then the immediate Fe(III)Fe(III) structure after $Tyr122^•$ is reduced. The calculated pK_a's for the processes

$$M(O_{br}, H_2O_{t2}) \rightarrow M(O_{br}, OH^-_{br}) + H^+ \quad (9)$$

and

$$M(O_{br}, H_2O_{t1}) \rightarrow M(O_{br}, OH^-_{br}) + H^+ \quad (10)$$

dx.doi.org/10.1021/ic1020127 |*Inorg. Chem.* 2011, 50, 2302–2320

are 13.36 and 13.87, respectively, showing that $M(O_{br},OH^{-}{}_{br})$ is less stable than $M(O_{br},H_2O_{t2})$ and $M(O_{br},H_2O_{t1})$. Later, the energy of the $M(O_{br},OH^{-}{}_{br})$ structure will be used to calculate the redox potential for reducing Tyr122$^{\bullet}$ starting from the transient $A(O_{br},OH^{-}{}_{br})$-Asp84H active state.

Further, in Figure 7e,f and columns e and f in Table 4, we present two more met diferric structures with deprotonated (negatively charged) Tyr122^{-}. Their diiron centers have the (O_{br},H_2O_{t2}) and (O_{br},H_2O_{t1}) forms, $M(O_{br},H_2O_{t2})$-Tyr122^{-} (Figure 7e) and $M(O_{br},H_2O_{t1})$-Tyr122^{-} (Figure 7f), respectively. The purpose of these two model calculations is to obtain the pK_a values of the −OH group of the Try122 side chain for the following processes:

$$M(O_{br}, H_2O_{t2}) \rightarrow M(O_{br}, H_2O_{t2})\text{-Tyr122}^{-} + H^{+} \quad (11)$$

and

$$M(O_{br}, H_2O_{t1}) \rightarrow M(O_{br}, H_2O_{t1})\text{-Tyr122}^{-} + H^{+} \quad (12)$$

To better estimate the term ΔZPE in eq 5 for the above processes, we optimized the geometries of the Tyr122 side chain alone in neutral and anion deprotonated forms within COSMO solvation model (ε = 20) and performed frequency calculations at the two optimized geometries. ΔZPE = −8.03 kcal mol^{-1} was obtained. The calculated pK_a's for processes (11) and (12) are given in Table 4 and will be used for calculation of the coupled redox potential for reducing the Tyr122$^{\bullet}$ radical from the active state to met diferric state in the following section.

The Fe−Fe distance of model $M(O_{br},H_2O_{t2})$ (3.192 Å) is by 0.04 Å longer than that of $A(O_{br},H_2O_{t1})$, and it is the longest among the met diferric models. The Fe−Fe distance in chain A of the X-ray crystal (2.2 Å resolution) structure is 3.42 and in chain B 3.29 Å.[3] Therefore, our calculated Fe−Fe distances in these met diferric models are at least 0.1 Å shorter than those in the experiment. One possible rationale for this and other geometric differences is that we did not fix the positions of the linking hydrogen atoms to the first-shell ligands in these geometry optimizations.

4.5. Relative Energies and Redox Potentials between Different States. Through experiments using various redox mediators, Silva et al. found that the (proton-coupled) redox potential ($E^{o\prime}$) for the active Tyr122$^{\bullet}$ radical (at pH 7.6 and 4 °C) is more positive than +0.64 V and more negative than +1.33 V vs SHE.[107] The redox potentials for amino acids in aqueous solutions and in peptides have also been measured.[108−110] In this section, we will present the relative energies and redox potentials between the different radical and oxidation states studied previously to see if we can produce reasonable results by our current DFT-OPBE calculations. First, we examine the coupled redox potentials for the following processes:

$$A(O_{br}, H_2O_{t2}) + e^{-} + H^{+} \rightarrow M(O_{br}, H_2O_{t2}) \quad (13)$$

and

$$A(O_{br}, H_2O_{t1}) + e^{-} + H^{+} \rightarrow M(O_{br}, H_2O_{t1}) \quad (14)$$

Each of them can be considered as two processes in series

$$A(O_{br}, H_2O_{t2}) + e^{-} \rightarrow M(O_{br}, H_2O_{t2})\text{-Tyr122}^{-} \quad (13a)$$

$$M(O_{br}, H_2O_{t2})\text{-Tyr122}^{-} + H^{+} \rightarrow M(O_{br}, H_2O_{t2}) \quad (13b)$$

and

$$A(O_{br}, H_2O_{t1}) + e^{-} \rightarrow M(O_{br}, H_2O_{t1})\text{-Tyr122}^{-} \quad (14a)$$

$$M(O_{br}, H_2O_{t1})\text{-Tyr122}^{-} + H^{+} \rightarrow M(O_{br}, H_2O_{t1}) \quad (14b)$$

The simple redox potential of eqs 13a and 14a can be calculated as in eqs 13c and 14c, respectively:

$$E^{\circ}(\text{eq 13a}) = E[A(O_{br}, H_2O_{t2})] - E[M(O_{br}, H_2O_{t2})\text{-Tyr122}^{-}] + \Delta\text{SHE} \quad (13c)$$

and

$$E^{\circ}(\text{eq 14a}) = E[A(O_{br}, H_2O_{t1})] - E[M(O_{br}, H_2O_{t1})\text{-Tyr122}^{-}] + \Delta\text{SHE} \quad (14c)$$

The BS state energies (E) of models $A(O_{br},H_2O_{t2})$, $M(O_{br},H_2O_{t2})$-Tyr122^{-}, $A(O_{br},H_2O_{t1})$, and $M(O_{br},H_2O_{t1})$-Tyr122^{-} are given in Tables 3 and 4. ΔSHE is the standard hydrogen electrode potential. Lewis et al. calculated ΔSHE = −4.28 V based solely on the experimental data.[91,92] They had included the free energy (−6.2 kJ mol^{-1} = −0.06 eV) of an electron at room temperature in their calculations. However, the reference energy in our redox calculations always sets the electron energy threshold as zero. The important point here is to be consistent in using the same reference energy. By setting $\Delta G^{\circ}_{f,298}(e^{-})$ = 0, the ΔSHE value calculated by Lewis et al. is then shifted by −0.06 V. That is, ΔSHE = −4.34 V, which is used in our current redox potential calculations. We then obtain E°(eq 13a) = 0.07 V and E°(eq 14a) = 0.04 V.

The coupled redox potentials of eqs 13 and 14 are then calculated according to eqs 13d and 14d, respectively:[111]

$$E^{o\prime}(\text{eq 13}) = E^{\circ}(\text{eq 13a}) + 1.37[\text{p}K_a(\text{eq 13b}) - \text{pH}]/23.06 \quad (13d)$$

and

$$E^{o\prime}(\text{eq 14}) = E^{\circ}(\text{eq 14a}) + 1.37[\text{p}K_a(\text{eq 14b}) - \text{pH}]/23.06 \quad (14d)$$

where pK_a(eq 13b) = 16.98 and pK_a(eq 14b) = 16.78 are given in Table 4. When pH 7.6, we have $E^{o\prime}$(eq 13) = 0.63 V and $E^{o\prime}$(eq 14) = 0.59 V. Combining the chemical reduction/oxidation observations with different redox mediators and the known ability of hydroxyurea (redox potential +0.73 V vs SHE) to reduce Tyr122$^{\bullet}$ yields an experimental redox potential range from +0.73 to +1.33 V (at pH 7.6 and 4 °C).[107] Our calculated redox potential range for the "resting" active states $A(O_{br},H_2O_{t2})$ and $A(O_{br},H_2O_{t1})$ is less positive than the lower bound by about 0.1−0.15 V.

On the other hand, if the $A(O_{br},OH^{-}{}_{br})$-Asp84H (Figure 6d) model represents the transient intermediate state facilitating the coupled e^{-}/H^{+} reduction of Tyr122$^{\bullet}$ for the radical (hole) transfer from subunit R2 to R1, the redox process (eq 15) starting from $A(O_{br},OH^{-}{}_{br})$-Asp84H provides another relevant coupled redox potential for reducing Tyr122$^{\bullet}$ in *E. coli* R2:

$$A(O_{br}, OH^{-}{}_{br})\text{-Asp84H} + e^{-} + H^{+} \rightarrow M(O_{br}, H_2O_{t1}) \quad (15)$$

dx.doi.org/10.1021/ic1020127 |*Inorg. Chem.* 2011, 50, 2302–2320

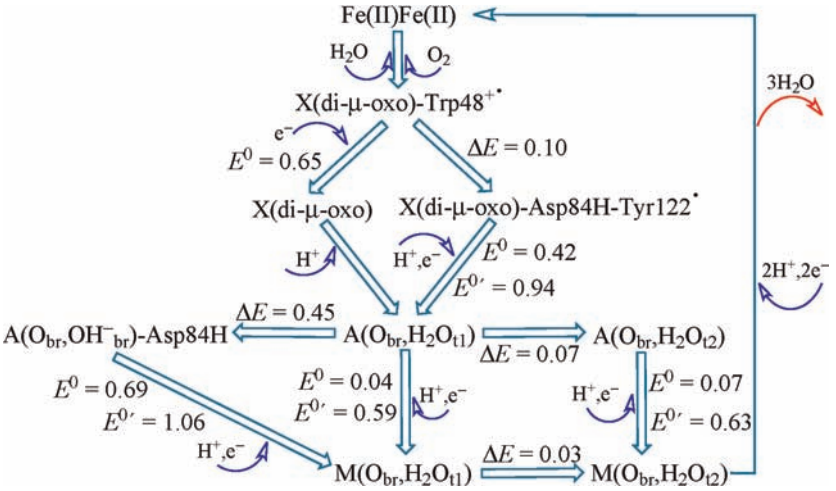

Figure 8. Schematic reaction cycle in *E. coli* RNR R2 shown with calculated relative energies (ΔE, eV), simple redox potentials ($E°$, V), and coupled redox potentials ($E°'$, V, at pH 7.6) between the typical oxidation and radical states. Both model X(di-μ-oxo) and model X(di-μ-oxo)-Trp48$^{\bullet+}$ are shown in Figure 2. Model X(di-μ-oxo)-Asp84H-Tyr122$^{\bullet}$ is shown in Figure 5a with protonated Asp84 side chain.

Again, this process can be written in the following two steps:

$$A(O_{br}, OH^{-}{}_{br})\text{-Asp84H} + e^{-} \rightarrow M(O_{br}, OH^{-}{}_{br}) \quad (15a)$$

$$M(O_{br}, OH^{-}{}_{br}) + H^{+} \rightarrow M(O_{br}, H_2O_{t1}) \quad (15b)$$

The simple redox potential of eq 15a can be calculated as

$$E°(\text{eq 15a}) = E[A(O_{br}, OH^{-}{}_{br})\text{-Asp84H}] - E[M(O_{br}, OH^{-}{}_{br})] + \Delta\text{SHE} = 0.69\ \text{V} \quad (15c)$$

The pK_a of process (15b) is 13.87 (Table 4). Therefore, the coupled redox potential for process 15 at pH 7.6 is

$$E°'(\text{eq 15}) = E°(\text{eq 15a}) + 1.37[pK_a(\text{eq 15b}) - \text{pH}]/23.06 = 1.06\ \text{V} \quad (15d)$$

This value agrees very well with the expected redox potential range typical for tyrosine.[107]

Other simple or coupled redox potentials that can be calculated are

$$X(\text{di-}\mu\text{-oxo})\text{-Trp48}^{\bullet+} + e^{-} \rightarrow X(\text{di-}\mu\text{-oxo}) \quad (16)$$

and

$$X(\text{di-}\mu\text{-oxo})\text{-Asp84H-Tyr122}^{\bullet} + e^{-} + H^{+} \rightarrow A(O_{br}, H_2O_{t1}) \quad (17)$$

The model cluster X(di-μ-oxo) shown in Figure 2 was already calculated and presented in our previous paper,[31] where it was named Model-B. The calculated geometric and Mössbauer properties of X(di-μ-oxo) with dielectric constant ε = 20 are given in Figure 4 of ref 31. Here we simply use this X(di-μ-oxo) model to calculate the redox potential of eq 16 (without protonation). The BS state energy of X(di-μ-oxo) directly after geometry optimization is E[X(di-μ-oxo)] = −885.6781 eV, which was not given in ref 31. With this energy and the S_{total} = 0 state X(di-μ-oxo)-Trp48$^{\bullet+}$ energy E[X(di-μ-oxo)-Trp48$^{\bullet+}$] = −880.6840 eV given in Table 1, the simple redox of eq 16 can be calculated as

$$E°(\text{eq 16}) = E[X(\text{di-}\mu\text{-oxo})\text{-Trp48}^{\bullet+}] - E[X(\text{di-}\mu\text{-oxo})] + \Delta\text{SHE} = 0.65\ \text{V} \quad (16a)$$

The experimental amino acid redox potential for the Trp$^{\bullet+}$/Trp couple in peptides and in an aqueous solution is around 1.15 V at pH 2 or 3.[108−110] However, this experimental value may not closely represent the redox potential of process (16) in protein R2.

Similar to processes (13) and (14), (17) can also be written in the following two steps:

$$X(\text{di-}\mu\text{-oxo})\text{-Asp84H-Tyr122}^{\bullet} + e^{-} \rightarrow A(O_{br}, OH^{-}{}_{br}) \quad (17a)$$

$$A(O_{br}, OH^{-}{}_{br}) + H^{+} \rightarrow A(O_{br}, H_2O_{t1}) \quad (17b)$$

The energies of X(di-μ-oxo)-Asp84H-Tyr122$^{\bullet}$ and A(O_{br}, $OH^{-}{}_{br}$) are given in Tables 2 and 3, respectively, and pK_a(eq 17b) = 16.29 is given in Table 3. Then the simple redox potential of (17a) can be calculated as

$$E°(\text{eq 17a}) = E[X(\text{di-}\mu\text{-oxo})\text{-Asp84H-Tyr122}^{\bullet}] - E[A(O_{br}, OH^{-}{}_{br})] + \Delta\text{SHE} = 0.42\ \text{V} \quad (17c)$$

and the coupled redox potential of eq 17 at pH 7.6 can be obtained as

$$E°'(\text{eq 17}) = E°(\text{eq 17a}) + 1.37[pK_a(\text{eq 17b}) - \text{pH}]/23.06 = 0.94\ \text{V} \quad (17d)$$

In Figure 8, we show the calculated relative energies (ΔE, eV), simple redox potentials ($E°$, V), and coupled redox potentials ($E°'$, V, at pH 7.6) between various oxidation and radical states during the catalytic cycle [starting with X(di-μ-oxo)-Trp48$^{\bullet+}$ and ending with the met Fe(III)Fe(III) state] in *E. coli* R2 obtained in the current study. The current calculations do not include vibrational entropy terms or the extended protein

dx.doi.org/10.1021/ic1020127 |*Inorg. Chem.* 2011, 50, 2302–2320

environment. However, the calculated redox potentials are still in reasonably good agreement with the experimental range.

4.6. Reaction Pathway Mechanisms and Energetics: Comparisons with Earlier Models. One important question is, what accounts for the stability of the tyrosine radical (Tyr122$^{\bullet}$) within subunit R2? In this respect, our models for X and for the activation reaction pathway producing the Tyr122$^{\bullet}$ radical are different from Siegbahn's.[23] Both proposals utilize Asp84 in proton transfer, but in Siegbahn's, there is an intervening added H_2O molecule. Siegbahn proposes in ref23 that the high exothermicity to go from X to the active (Tyr122$^{\bullet}$) state explains the stability of Tyr122. In our view, this result is only suggestive and not at all sufficient because this proposal does not address the coupled electron/proton reduction proceeding from the active form (A, having Fe(III)Fe(III)-Tyr122$^{\bullet}$) to the met state (M, having Fe(III)Fe(III)-Tyr122-OH). We think that the comparative redox potentials for the activation process (1) X-Trp48$^{\bullet+}$ + $e^- + H^+ \rightarrow$ A versus (2) A + $e^- + H^+ \rightarrow$ M are more relevant because for (2) the redox potential $E^{o\prime}$ is about 0.25 V less positive than that for (1), so the driving force for reduction from an external one-electron donor (external reductant) is less (Figure 8). Probably even more important is control on the redox potential by limiting proton access into the active site because the redox potential is about 0.5 V less positive for E° (without proton transfer) compared to $E^{o\prime}$ (with proton transfer). Therefore, kinetic control of protons entering the active site can keep the active state A from being reduced to M(met). We do not know all of the conformational changes between A and M, and the electron tunneling as well as the proton-transfer barriers may be different. Therefore, the kinetics of proton transfer can play an important role in the stability of Tyr122$^{\bullet}$. The hyperactive state A(O_{br},OH^-_{br})-Asp84H (Figure 6d) has a higher redox potential to M, which makes it more vulnerable to reduction, but its equilibrium concentration is correspondingly much less than that of A, by a calculated factor of about $10^{-7.6}$. In Stubbe and coworkers' model[112] for the kinetic mechanism of the catalytic cycle, most steps involve subunit R2 docked to R1, and therefore these will provide considerable protection of Tyr122$^{\bullet}$ against electron transfer from external reductants. However, the substrate-free form of subunit R1, after disulfide rereduction, is proposed to require dissociation of R2 from R1, leaving Tyr122$^{\bullet}$ much more accessible to the reductant once per turnover. In the activation cycle as well, R2 is separated from R1, but this is a much rarer event.

A second important question is, why and how does radical transfer occur on the catalytic pathway starting from Tyr122$^{\bullet}$ (on subunit R2) when the substrate is bound to subunit R1? This question has two parts: the first involves long-range electron transfer via a combined multistep electron tunneling process, and the second involves the local initiation of radical transfer within subunit R2. We will address only the second part here, noting that there are long-range effects also from the driving force of Cys439 thiolate oxidation, from subunit R2 binding to R1, and from conformational changes, affecting both the dielectric environment and charge distribution. In any event, we will consider the initial steps in radical transfer on the catalytic pathway from the active Tyr122$^{\bullet}$ state to generate the Trp48$^{\bullet+}$ cation radical. Here our proposed mechanism differs even qualitatively from Siegbahn's.[23] We propose that Asp84 acts as a proton-transfer conduit from the bridging H_2O, providing a preorganized, although transient state for coupled e^-/H^+ transfer to Tyr122$^{\bullet}$ from Trp48. This is essentially like the reverse of our proposed Tyr122$^{\bullet}$ activation pathway. Siegbahn proposes instead a proton-transfer pathway from a H_2O-bound terminal to Fe1 after an initial external proton transfer to the diferric cluster, so these mechanisms are quite different. In Stubbe's kinetic model,[112] the estimated rate constant for electron transfer from Cys439 to Tyr122 is greater than 1000 s^{-1}, which is consistent (at 300 K) with a barrier or a series of barriers of about 14 kcal mol^{-1} or less based on standard transition state theory. (This result will be modified by the electron-transfer rate prefactor, which includes the electron tunneling factor $2\pi^{3/2}(H_{AD}{}^2)/[\lambda^{1/2}(RT)^{3/2}]$.[113] Our predicted equilibrium energy for the hyperactive state A(O_{br},OH^-_{br})-Asp84H (Figure 6d) is about 10.4 kcal mol^{-1} above that of the resting Tyr122$^{\bullet}$ state A(O_{br},H_2O_{t1}) (Figure 6b). The barrier to A(O_{br},OH^-_{br})-Asp84H must be higher than this value, but we have not yet evaluated it or the net barrier and net energy change for the coupled electron/proton transfer generating Trp48$^{\bullet+}$ and Tyr122-OH. In Siegbahn's proposed pathway, ΔE for producing Trp48$^{\bullet+}$ and Tyr122-OH is 3.9 kcal mol^{-1} with external proton transfer and 11.8 kcal mol^{-1} without it. The cost of initial external proton transfer to the active-site cluster is not determined. We think that our mechanism is simpler and more direct than the one Siegbahn has proposed, and in our mechanism, Asp84 acts as a proton-transfer conduit in both the tyrosine radical activation and the catalytic radical-transfer pathways. However, there are many open questions about the catalytic radical-transfer pathway, and considerable additional work is needed to attain a more complete picture of this mechanism.

5. CONCLUSIONS

Active-site models for class Ia *E. coli* R2 in X{Fe1(III)Fe2(IV)}-Trp48$^{\bullet+}$, X{Fe1(III)Fe2(IV)}-Tyr122$^{\bullet}$, active Fe1(III)Fe2(III)-Tyr122$^{\bullet}$, and met Fe1(III)Fe2(III) states have been examined for structures, energies, and properties, using BS DFT methodology. Different structural isomers and different protonation states have been explored. The proposed transient Fe(IV)Fe(IV) state is also examined.

Combining our current and Siegbahn's previous calculations and the experimental observations,[23,24] both Trp48 and Asp84 in *E. coli* R2 are the important contributing factors for class Ia RNR and MMOH behaving differently upon O_2 binding with the Fe(II)Fe(II) center. The steric strain of the short Asp84 side chain in RNR generates an energy cost when Fe1 and Fe2 move closer, which is likely why the cis-μ-1,2 type[41,42] peroxo intermediate state is not observed in wild-type R2 but observed in MMOH[42,95,114] and in the D84E mutant R2.[39] Because of the long Fe(II)−Fe(II) distance, the peroxo intermediate in wild-type R2 would easily change from cis to trans or μ-η^2,η^2 form to facilitate O−O bond cleavage. In fact, O_2 may directly bind in a trans or μ-η^2,η^2 form in wild-type R2 because the peroxo-Fe(III)Fe(III) complex has to decay rapidly.[11] Electron transfer from Trp48 to Fe1 in R2 possibly occurs sometime during O−O bond cleavage, which explains why O−O bond cleavage in the W48F mutant is much slower [80 s^{-1} for the formation of the Fe(IV)Fe(IV) species][12] than in wild-type R2 (200 s^{-1} for the formation of the X-Trp48$^{\bullet+}$ state).[11] For the portion of O−O bond cleavage that happens before electron transfer from Trp48 to Fe1, the steric strain of Asp84 hinders the decrease of the Fe1−Fe2 distance to attain the lowest-energy structure of the Fe(IV)Fe(IV) state. Rather, the active site compresses to a geometry that is similar to that of the X(di-μ-oxo)-Trp48$^{\bullet+}$

dx.doi.org/10.1021/ic1020127 |*Inorg. Chem.* 2011, 50, 2302–2320

state, where one electron transfers from Trp48 to Fe1. This provides another reason that the Fe(IV)Fe(IV) state is not observed in wild-type *E. coli* R2, in contrast to MMO.

Turning now to the X, active, and met species, we develop a detailed assessment of tautomeric states, as shown in Figures 5–8. Protonated Asp84H plays a critical role as a proton-transfer conduit between the diiron cluster and Tyr122$^{\bullet}$. Asp84 is essential both in the activation process for generating the Tyr122$^{\bullet}$ radical state and in the catalytic pathway after activation. There are three particularly important active states: (a) A(O_{br},H_2O_{t2}), (b) A(O_{br},H_2O_{t1}), and (d) A(O_{br},OH^-_{br})-Asp84H (Figure 6a,b,d and Table 3). The first two are low-lying "resting" active states corresponding to the stable Tyr122$^{\bullet}$ radical observed spectroscopically. The last (d) A(O_{br},OH^-_{br})-Asp84H is calculated to lie 0.45 eV (10.4 kcal mol^{-1}) higher in energy than active model b. Model d is a highly transient, hyperactive catalytic species ready to oxidize Trp48 to Trp48$^{\bullet+}$ to start the catalytic cycle of hole transfer from subunit R2 to the catalytic substrate binding site on subunit R1, where a Cys radical is generated. The proton on Asp84H is very well positioned for immediate proton transfer for the reduction of Tyr122$^{\bullet}$. From the calculated energy difference between A(O_{br},OH^-_{br})-Asp84H [model A(d)] and A(O_{br},H_2O_{t1}) [model A(b)], we can estimate a relative equilibrium constant of [A(d)]/[A(b)] = $10^{-7.6}$. So while structure A(b) is stable, A(d) is present only about 100 μs h^{-1}.

In Figure 8, the calculated proton-coupled redox potential ($E^{o\prime}$) for X(di-μ-oxo)-Asp84H-Tyr122$^{\bullet}$ → A(O_{br},H_2O_{t1}) and the three $E^{o\prime}$ values from active (A) to met RNR-R2 (M) are 0.4–0.6 V more positive than the corresponding simple electron-transfer redox potentials (E^{o}). Therefore, kinetic control of proton transfer to the diiron center or to Tyr122$^{\bullet}$ plays a critical role for the occurrence of these processes. When Tyr122$^{\bullet}$ has been generated in the "resting" active state(s) [A(a) and A(b)], it is blocked by the side chain of Phe208. There is possibly no available proton-transfer source and path nearby. Therefore, Tyr122$^{\bullet}$ in the active state can stay for days at room temperature.[1] It is likely that, because the docking of R1 and R2 provides the source and pathway of proton (and electron) transfer, Tyr122$^{\bullet}$ is then reduced and the radical transfers to R1.[23] The proposed electron-coupled proton-transfer pathway between Tyr122$^{\bullet}$ in R2 and Cys439 in R1 contains the residues His118, Asp237, Trp48, and Tyr356 in R2 and Tyr731 and Tyr730 in R1.[115]

The current work provides a clear framework for further progress in understanding the intricate mechanisms of radical activation and catalysis in diiron RNR.

■ ASSOCIATED CONTENT

Supporting Information. Some optimized active-site model geometries. This material is available free of charge via the Internet at http://pubs.acs.org.

■ AUTHOR INFORMATION

Corresponding Author
*E-mail: lou@scripps.edu. Fax: (858) 784-8896.

■ ACKNOWLEDGMENT

We thank the NIH for financial support (Grant GM043278 to L.N.). The support of computer resources of the Scripps Research Institute is also gratefully acknowledged.

■ REFERENCES

(1) Wallar, B. J.; Lipscomb, J. D. *Chem. Rev.* **1996**, *96*, 2625–2658.
(2) Sjöberg, B. M. *Struct. Bonding (Berlin)* **1997**, *88*, 139–173.
(3) Nordlund, P.; Eklund, H. *J. Mol. Biol.* **1993**, *232*, 123–164.
(4) Logan, D. T.; Su, X. D.; Aberg, A.; Regnstrom, K.; Hajdu, J.; Eklund, H.; Nordlund, P. *Structure* **1996**, *4*, 1053–1064.
(5) Bollinger, J. M., Jr.; Edmondson, D. E.; Huynh, B. H.; Filley, J.; Norton, J. R.; Stubbe, J. *Science* **1991**, *253*, 292–298.
(6) Bollinger, J. M., Jr.; Stubbe, J.; Huynh, B. H.; Edmondson, D. E. *J. Am. Chem. Soc.* **1991**, *113*, 6289–6291.
(7) Ravi, N.; Bollinger, J. M., Jr.; Huynh, B. H.; Edmondson, D. E.; Stubbe, J. *J. Am. Chem. Soc.* **1994**, *116*, 8007–8014.
(8) Ravi, N.; Bominaar, E. L. *Inorg. Chem.* **1995**, *34*, 1040–1043.
(9) Bollinger, J. M., Jr.; Tong, W. H.; Ravi, N.; Huynh, B. H.; Edmondson, D. E.; Stubbe, J. In *Methods in Enzymolology*; Klinman, J. P., Ed.; Academic Press: New York, 1995; p 258.
(10) Sturgeon, B. E.; Burdi, D.; Chen, S. X.; Huynh, B. H.; Edmondson, D. E.; Stubbe, J.; Hoffman, B. M. *J. Am. Chem. Soc.* **1996**, *118*, 7551–7557.
(11) Baldwin, J.; Krebs, C.; Ley, B. A.; Edmondson, D. E.; Huynh, B. H.; Bollinger, J. H. *J. Am. Chem. Soc.* **2000**, *122*, 12195–12206.
(12) Krebs, C.; Chen, S. X.; Baldwin, J.; Ley, B. A.; Patel, U.; Edmondson, D. E.; Huynh, B. H.; Bollinger, J. M. *J. Am. Chem. Soc.* **2000**, *122*, 12207–12219.
(13) Bollinger, J. M.; Tong, W. H.; Ravi, N.; Huynh, B. H.; Edmondson, D. E.; Stubbe, J. *J. Am. Chem. Soc.* **1994**, *116*, 8015–8023.
(14) Bollinger, J. M.; Tong, W. H.; Ravi, N.; Huynh, B. H.; Edmondson, D. E.; Stubbe, J. *J. Am. Chem. Soc.* **1994**, *116*, 8024–8032.
(15) Burdi, D.; Sturgeon, B. E.; Tong, W. H.; Stubbe, J. A.; Hoffman, B. M. *J. Am. Chem. Soc.* **1996**, *118*, 281–282.
(16) Veselov, A.; Scholes, C. P. *Inorg. Chem.* **1996**, *35*, 3702–3705.
(17) Willems, J. P.; Lee, H. I.; Burdi, D.; Doan, P. E.; Stubbe, J.; Hoffman, B. M. *J. Am. Chem. Soc.* **1997**, *119*, 9816–9824.
(18) Riggs-Gelasco, P. J.; Shu, L. J.; Chen, S. X.; Burdi, D.; Huynh, B. H.; Que, L.; Stubbe, J. *J. Am. Chem. Soc.* **1998**, *120*, 849–860.
(19) Burdi, D.; Willems, J.-P.; Riggs-Gelasco, P.; Antholine, W. E.; Stubbe, J.; Hoffman, B. M. *J. Am. Chem. Soc.* **1998**, *120*, 12910–12919.
(20) Shanmugam, M.; Doan, P. E.; Lees, N. S.; Stubbe, J.; Hoffman, B. M. *J. Am. Chem. Soc.* **2009**, *131*, 3370–3376.
(21) Mitić, N.; Saleh, L.; Schenk, G.; Bollinger, J. M. J.; Solomon, E. I. *J. Am. Chem. Soc.* **2003**, *125*, 11200–11201.
(22) Siegbahn, P. E. M. *Inorg. Chem.* **1999**, *38*, 2880–2889.
(23) Siegbahn, P. E. M. *Q. Rev. Biophys.* **2003**, *36*, 91–145.
(24) Siegbahn, P. E. M. *Chem. Phys. Lett.* **2002**, *351*, 311–318.
(25) Han, W.-G.; Lovell, T.; Liu, T.; Noodleman, L. *Inorg. Chem.* **2003**, *42*, 2751–2758.
(26) Han, W.-G.; Lovell, T.; Liu, T.; Noodleman, L. *Inorg. Chem.* **2004**, *43*, 613–621.
(27) Han, W. G.; Liu, T. Q.; Lovell, T.; Noodleman, L. *J. Am. Chem. Soc.* **2005**, *127*, 15778–15790.
(28) Han, W.-G.; Liu, T.; Lovell, T.; Noodleman, L. *Inorg. Chem.* **2006**, *45*, 8533–8542.
(29) Han, W.-G.; Liu, T.; Lovell, T.; Noodleman, L. *J. Inorg. Biochem.* **2006**, *100*, 771–779.
(30) Han, W.-G.; Noodleman, L. *Dalton Trans.* **2009**, 6045–6057.
(31) Han, W.-G.; Noodleman, L. *Theor. Chem. Acc.* **2010**, *125*, 305–317.
(32) Younker, J. M.; Krest, C. M.; Jiang, W.; Krebs, C.; Bollinger, J. M.; Green, M. T. *J. Am. Chem. Soc.* **2008**, *130*, 15022–15027.
(33) Jiang, W.; Yun, D.; Saleh, L.; Bollinger, J. M.; Krebs, C. *Biochemistry* **2008**, *47*, 13736–13744.
(34) Jiang, W.; Saleh, L.; Barr, E. W.; Xie, J. J.; Gardner, M. M.; Krebs, C.; Bollinger, J. M. *Biochemistry* **2008**, *47*, 8477–8484.
(35) Mitić, N.; Clay, M. D.; Saleh, L.; Bollinger, J. M. J.; Solomon, E. I. *J. Am. Chem. Soc.* **2007**, *129*, 9049–9065.
(36) Noodleman, L. *J. Chem. Phys.* **1981**, *74*, 5737–5743.
(37) Noodleman, L.; Case, D. A. *Adv. Inorg. Chem.* **1992**, *38*, 423–470.

(38) Noodleman, L.; Lovell, T.; Han, W.-G.; Liu, T.; Torres, R. A.; Himo, F. . In *Comprehensive Coordination Chemistry II, From Biology to Nanotechnology*; Lever, A. B., Ed.; Elsevier Ltd.: New York, 2003; Vol. 2, pp 491−510.
(39) Moenne-Loccoz, P.; Baldwin, J.; Ley, B. A.; Loehr, T. M.; Bollinger, J. M. *Biochemistry* **1998**, *37*, 14659–14663.
(40) Baldwin, J.; Voegtli, W. C.; Khidekel, N.; Moenne-Loccoz, P.; Krebs, C.; Pereira, A. S.; Ley, B. A.; Huynh, B. H.; Loehr, T. M.; Riggs-Gelasco, P. J.; Rosenzweig, A. C.; Bollinger, J. M. *J. Am. Chem. Soc.* **2001**, *123*, 7017–7030.
(41) Jensen, K. P.; Bell, C. B.; Clay, M. D.; Solomon, E. I. *J. Am. Chem. Soc.* **2009**, *131*, 12155–12171.
(42) Han, W.-G.; Noodleman, L. *Inorg. Chem.* **2008**, *47*, 2975–2986.
(43) Saleh, L.; Krebs, C.; Ley, B. A.; Naik, S.; Huynh, B. H.; Bollinger, J. M. *Biochemistry* **2004**, *43*, 5953–5964.
(44) Han, W.-G.; Tajkhorshid, E.; Suhai, S. *J. Biomol. Struct. Dyn.* **1999**, *16*, 1019–1032.
(45) Bollinger, J. M.; Chen, S. X.; Parkin, S. E.; Mangravite, L. M.; Ley, B. A.; Edmondson, D. E.; Huynh, B. H. *J. Am. Chem. Soc.* **1997**, *119*, 5976–5977.
(46) ADF2008.01 Amsterdam Density Functional Software, SCM, Theoretical Chemistry, Vrije Universiteit, Amsterdam, The Netherlands, http://www.scm.com.
(47) te Velde, G.; Bickelhaupt, F. M.; Baerends, E. J.; Guerra, C. F.; Van Gisbergen, S. J. A.; Snijders, J. G.; Ziegler, T. *J. Comput. Chem.* **2001**, *22*, 931–967.
(48) Guerra, C. F.; Snijders, J. G.; te Velde, G.; Baerends, E. J. *Theor. Chem. Acc.* **1998**, *99*, 391–403.
(49) Vosko, S. H.; Wilk, L.; Nusair, M. *Can. J. Phys.* **1980**, *58*, 1200–1211.
(50) Perdew, J. P.; Burke, K.; Ernzerhof, M. *Phys. Rev. Lett.* **1996**, *77*, 3865–3868.
(51) Perdew, J. P.; Burke, K.; Ernzerhof, M. *Phys. Rev. Lett.* **1997**, *78*, 1396–1396.
(52) Handy, N. C.; Cohen, A. J. *Mol. Phys.* **2001**, *99*, 403–412.
(53) Perdew, J. P.; Chevary, J. A.; Vosko, S. H.; Jackson, K. A.; Pederson, M. R.; Singh, D. J.; Fiolhais, C. *Phys. Rev. B* **1992**, *46*, 6671–6687.
(54) Han, W. G.; Noodleman, L. *Inorg. Chim. Acta* **2008**, *361*, 973–986.
(55) Swart, M.; Groenhof, A. R.; Ehlers, A. W.; Lammertsma, K. *J. Phys. Chem. A* **2004**, *108*, 5479–5483.
(56) Swart, M.; Ehlers, A. W.; Lammertsma, K. *Mol. Phys.* **2004**, *102*, 2467–2474.
(57) Becke, A. D. *Phys. Rev. A* **1988**, *38*, 3098–3100.
(58) Lee, C. T.; Yang, W. T.; Parr, R. G. *Phys. Rev. B* **1988**, *37*, 785–789.
(59) Perdew, J. P. *Phys. Rev. B* **1986**, *33*, 8822–8824.
(60) Perdew, J. P. *Phys. Rev. B* **1986**, *34*, 7406–7406.
(61) Grimme, S. *J. Chem. Phys.* **2006**, *124*, 034108.
(62) Staroverov, V. N.; Scuseria, G. E.; Tao, J. M.; Perdew, J. P. *J. Chem. Phys.* **2003**, *119*, 12129–12137.
(63) Becke, A. D. *J. Chem. Phys.* **1993**, *98*, 5648–5652.
(64) Hertwig, R. H.; Koch, W. *Chem. Phys. Lett.* **1997**, *268*, 345–351.
(65) Jensen, K. P. *Inorg. Chem.* **2008**, *47*, 10357–10365.
(66) Furche, F.; Perdew, J. P. *J. Chem. Phys.* **2006**, *124*, 044103.
(67) Orio, M.; Pantazis, D. A.; Petrenko, T.; Neese, F. *Inorg. Chem.* **2009**, *48*, 7251–7260.
(68) Ye, S. F.; Neese, F. *Inorg. Chem.* **2010**, *49*, 772–774.
(69) Klamt, A.; Schüürmann, G. *J. Chem. Soc., Perkin Trans. 2* **1993**, 799–805.
(70) Klamt, A. *J. Phys. Chem.* **1995**, *99*, 2224–2235.
(71) Klamt, A.; Jonas, V. *J. Chem. Phys.* **1996**, *105*, 9972–9981.
(72) Pye, C. C.; Ziegler, T. *Theor. Chem. Acc.* **1999**, *101*, 396–408.
(73) Gregg, E. C. . *Handbook of Chemistry and Physics*; Chemical Rubber Company: Cleveland, OH, 1976; pp E55−E60.
(74) Harvey, S. C.; Hoekstra, P. *J. Phys. Chem.* **1972**, *76*, 2987–2994.
(75) Bone, S.; Pethig, R. *J. Mol. Biol.* **1982**, *157*, 571–575.
(76) Bone, S.; Pethig, R. *J. Mol. Biol.* **1985**, *181*, 323–326.
(77) Dwyer, J. J.; Gittis, A. G.; Karp, D. A.; Lattman, E. E.; Spencer, D. S.; Stites, W. E.; Garcia-Moreno, B. *Biophys. J.* **2000**, *79*, 1610–1620.
(78) Sham, Y. Y.; Muegge, I.; Warshel, A. *Biophys. J.* **1998**, *74*, 1744–1753.
(79) Bashford, D.; Karplus, M. *Biochemistry* **1990**, *29*, 10219–10225.
(80) Fitch, C. A.; Karp, D. A.; Lee, K. K.; Stites, W. E.; Lattman, E. E.; Garcia-Moreno, B. *Biophys. J.* **2002**, *82*, 3289–3304.
(81) Antosiewicz, J.; McCammon, J. A.; Gilson, M. K. *Biochemistry* **1996**, *35*, 7819–7833.
(82) Simonson, T.; Brooks, C. L. *J. Am. Chem. Soc.* **1996**, *118*, 8452–8458.
(83) Karp, D. A.; Gittis, A. G.; Stahley, M. R.; Fitch, C. A.; Stites, W. E.; Garcia-Moreno, B. *Biophys. J.* **2007**, *92*, 2041–2053.
(84) Harms, M. J.; Schlessman, J. L.; Chimenti, M. S.; Sue, G. R.; Damjanovic, A.; Garcia-Moreno, B. *Protein Sci.* **2008**, *17*, 833–845.
(85) Oglezneva, I. M. *Russ. J. Coord. Chem.* **2009**, *35*, 711–719.
(86) Paulsen, H.; Trautwein, A. X. *J. Phys. Chem. Solids* **2004**, *65*, 793–798.
(87) Jensen, K. P.; Cirera, J. *J. Phys. Chem. A* **2009**, *113*, 10033–10039.
(88) Han, W.-G.; Liu, T.; Lovell, T.; Noodleman, L. *J. Comput. Chem.* **2006**, *27*, 1292–1306.
(89) Martinez-Pinedo, G.; Schwerdtfeger, P.; Caurier, E.; Langanke, K.; Nazarewicz, W.; Sohnel, T. *Phys. Rev. Lett.* **2001**, *87*, 062701(1−4).
(90) Tissandier, M. D.; Cowen, K. A.; Feng, W. Y.; Gundlach, E.; Cohen, M. H.; Earhart, A. D.; Coe, J. V.; Tuttle, T. R. *J. Phys. Chem. A* **1998**, *102*, 7787–7794.
(91) Lewis, A.; Bumpus, J. A.; Truhlar, D. G.; Cramer, C. J. *J. Chem. Educ.* **2004**, *81*, 596–604.
(92) Lewis, A.; Bumpus, J. A.; Truhlar, D. G.; Cramer, C. J. *J. Chem. Educ.* **2007**, *84*, 934.
(93) Tawa, G. J.; Topol, I. A.; Burt, S. K.; Caldwell, R. A.; Rashin, A. A. *J. Chem. Phys.* **1998**, *109*, 4852–4863.
(94) Elango, N.; Radhakrishnan, R.; Froland, W. A.; Wallar, B. J.; Earhart, C. A.; Lipscomb, J. D.; Ohlendorf, D. H. *Protein Sci.* **1997**, *6*, 556–568.
(95) Lee, S. Y.; Lipscomb, J. D. *Biochemistry* **1999**, *38*, 4423–4432.
(96) Lee, S. K.; Fox, B. G.; Froland, W. A.; Lipscomb, J. D.; Münck, E. *J. Am. Chem. Soc.* **1993**, *115*, 6450–6451.
(97) Liu, K. E.; Valentine, A. M.; Wang, D. L.; Huynh, B. H.; Edmondson, D. E.; Salifoglou, A.; Lippard, S. J. *J. Am. Chem. Soc.* **1995**, *117*, 10174–10185.
(98) Shu, L. J.; Nesheim, J. C.; Kauffmann, K.; Munck, E.; Lipscomb, J. D.; Que, L. *Science* **1997**, *275*, 515–518.
(99) Hsu, H. F.; Dong, Y. H.; Shu, L. J.; Young, V. G.; Que, L. *J. Am. Chem. Soc.* **1999**, *121*, 5230–5237.
(100) Gherman, B. F.; Dunietz, B. D.; Whittington, D. A.; Lippard, S. J.; Friesner, R. A. *J. Am. Chem. Soc.* **2001**, *123*, 3836–3837.
(101) Baik, M. H.; Newcomb, M.; Friesner, R. A.; Lippard, S. J. *Chem. Rev.* **2003**, *103*, 2385–2419.
(102) Högbom, M.; Huque, Y.; Sjöberg, B. M.; Nordlund, P. *Biochemistry* **2002**, *41*, 1381–1389.
(103) Åberg, A.; Nordlund, P.; Eklund, H. *Nature* **1993**, *361*, 276–278.
(104) Atkin, C. L.; Thelande, L; Reichard, P.; Lang, G. *J. Biol. Chem.* **1973**, *248*, 7464–7472.
(105) Lynch, J. B.; Juarez-Garcia, C.; Münck, E.; Que, L., Jr. *J. Biol. Chem.* **1989**, *264*, 8091–8096.
(106) Sahlin, M.; Ehrenberg, A.; Graslund, A.; Sjoberg, B. M. *J. Biol. Chem.* **1986**, *261*, 2778–2780.
(107) Silva, K. E.; Elgren, T. E.; Que, L.; Stankovich, M. T. *Biochemistry* **1995**, *34*, 14093–14103.
(108) Harriman, A. *J. Phys. Chem.* **1987**, *91*, 6102–6104.
(109) Defelippis, M. R.; Murthy, C. P.; Broitman, F.; Weinraub, D.; Faraggi, M.; Klapper, M. H. *J. Phys. Chem.* **1991**, *95*, 3416–3419.
(110) Stubbe, J.; van der Donk, W. A. *Chem. Rev.* **1998**, *98*, 705–762.

(111) Han, W.-G.; Lovell, T.; Noodleman, L. *Inorg. Chem.* **2002**, *41*, 205–218.
(112) Stubbe, J.; Nocera, D. G.; Yee, C. S.; Chang, M. C. Y. *Chem. Rev.* **2003**, *103*, 2167–2201.
(113) Reece, S. Y.; Nocera, D. G. *Annu. Rev. Biochem.* **2009**, *78*, 673–699.
(114) Valentine, A. M.; Stahl, S. S.; Lippard, S. J. *J. Am. Chem. Soc.* **1999**, *121*, 3876–3887.
(115) Stubbe, J.; Riggs-Gelasco, P. *Trends Biochem. Sci.* **1998**, *23*, 438–443.

■ NOTE ADDED AFTER ASAP PUBLICATION

This paper was published on the Web on February 15, 2011, with an an error in equation 17a. The corrected version was reposted on February 18, 2011.